

Article

Optical and Thermodynamic Investigations of a Methane- and Hydrogen-Blend-Fueled Large-Bore Engine Using a Fisheye Optical System

Stephan Karmann ^{1,*}, Stefan Eicheldinger ², Maximilian Prager ², Malte Jaensch ² and Georg Wachtmeister ¹¹ Institute of Internal Combustion Engines, Technical University of Munich, 80333 Munich, Germany² Institute of Sustainable Mobile Drivetrains, Technical University of Munich, 80333 Munich, Germany

* Correspondence: karmann@lvk.mw.tum.de

Abstract: The following paper presents thermodynamic and optical investigations of hydrogen-enriched methane combustion, showing the potential of a hydrogen admixture as a means to decarbonize stationary power generation. The optical investigations are carried out through a fisheye optical system directly mounted into the combustion chamber, replacing one exhaust valve. All of the tests were carried out with constant fuel energy producing 16 bar indicated mean effective pressure. The engine under investigation is a port-fueled 4.8 L single-cylinder large-bore research engine. The test series compared the differences between a conventional spark plug and an unscavenged pre-chamber spark plug as an ignition system. The fuel blends under investigation are 5 and 10%_v hydrogen mixed with methane and pure natural gas acting as a reference fuel. The thermodynamic results show a beneficial influence of the hydrogen admixture on both ignition systems and for all variations concerning the lean running limit, combustion stability and indicated efficiency, with the most significant influence being visible for the tests using conventional spark plugs. With the unscavenged pre-chamber spark plug and the combustion of the 10%_v hydrogen admixture, an increase in the indicated efficiency of 0.8% compared to NG is achievable. The natural chemiluminescence intensity traces were observed to be predominantly influenced by the air–fuel equivalence ratio. This results in a 20% higher intensity for the unscavenged pre-chamber spark plug for the combustion of 10%_v hydrogen compared to the conventional spark plug. This is also visible in the evaluations of the flame color derived from the dewarped combustion image series. The investigation of the torch flames also shows a difference in the air–fuel equivalence ratio but not between the different fuels. The results encourage the development of hydrogen-based fuels and the potential to store surplus sustainable energy in the form of hydrogen in existing gas grids.

Keywords: optical engine; large-bore engine; hydrogen–methane blend; port fuel injection; fisheye optic

Citation: Karmann, S.; Eicheldinger, S.; Prager, M.; Jaensch, M.; Wachtmeister, G. Optical and Thermodynamic Investigations of a Methane- and Hydrogen-Blend-Fueled Large-Bore Engine Using a Fisheye Optical System. *Energies* **2023**, *16*, 1590. <https://doi.org/10.3390/en16041590>

Academic Editor: Bjørn H. Hjertager

Received: 14 January 2023

Revised: 31 January 2023

Accepted: 1 February 2023

Published: 5 February 2023



Copyright: © 2023 by the authors. Licensee MDPI, Basel, Switzerland. This article is an open access article distributed under the terms and conditions of the Creative Commons Attribution (CC BY) license (<https://creativecommons.org/licenses/by/4.0/>).

1. Introduction

Sustainable energy production is a key issue in reducing the extent of climate change. For up to 150 years, the internal combustion engine (ICE) has been a key enabling technology for mobile and stationary power generation whilst being continuously optimized and improved. Thereby 25% of the world's power demand is satisfied through the use of ICEs, producing 10% of the world's greenhouse emissions (cf. [1]). Even with the increasing electrification of mobility, the ICE is a promising technology in the environment of Power to X. Hereby, surplus green energy provided by solar and wind sources is used to produce sustainable liquid fuels, such as oxymethylene ethers [2–5], or gaseous fuels, such as methane, hydrogen, and blends for storage and distribution. Onorati et al. [6] emphasize the possibilities of hydrogen in ICEs for sustainable energy production as well as the need for further investigations, especially regarding hydrogen and derived synthetic fuels. As of now, in the field of large-bore engines, these investigations are still rare (cf. [7]) but not of

less importance, as these engines are used for stationary power supply and are the driving force of freight transportation.

To provide the means for such investigations, a new kind of optical accessibility for large-bore engines was developed (cf. [8]), realized (cf. [9]), improved (cf. [10]) and presented in the following to investigate the combustion process of hydrogen methane blends. The admixture of hydrogen to methane is promising in many aspects regarding the optimization of the different fuel properties summarized in Table 1. The high stability of the tetrahedral molecule structure of methane causes its high stability and, therefore, its lower ignitability, whereas hydrogen is highly ignitable, improving the ignitability of mixtures. This results in improved lean-running conditions (cf. [7,11–15]). Additionally, with the increased admixture of hydrogen, the probability of abnormal combustion increases due to the higher ignitability of hydrogen. With the following investigated low admixture of 5 and 10%_v, these drawbacks are negligible, as [7] already shown, and as the following results will state. Therefore, these amounts tend to be a suitable way in the short- and mid-term timespan to replace fossil natural gas and can possibly be stored in natural gas grids. Further, the high laminar burning velocity of hydrogen improves combustion efficiency and the lean-running limits of fuel blends in contrast to the low laminar burning velocity of pure methane (cf. [7,11–14]). Due to the lower carbon-to-hydrogen ratio of the fuel blends, the CO₂ emission decreases, which is further supported by more stable lean-running combustion. One drawback of the admixture of hydrogen is the higher adiabatic flame temperature of hydrogen, resulting in increased NO_x emissions, especially for higher amounts of hydrogen admixture (cf. [7,11–14]).

Table 1. Fuel properties under normal conditions (cf. [16].)

Fuel Properties	H ₂	CH ₄
Density in kg/m ³	0.08	0.65
Ignitability in air in % _v	4–75	5–15
Auto ignition temperature in air in K	858	813
Minimum ignition energy in mJ	0.02	0.28
Laminar burning velocity in m/s	1.85	0.38
Adiabatic flame temperature in K at $\lambda = 1$	2390	2226
Quenching distance in mm	0.64	2.03

The combustion of hydrogen/methane mixtures basically follows the chemical reaction process of methane, altered in the elementary reaction steps according to the content of hydrogen and the combustion conditions (cp. [17]). Figure 1 shows the flame spectrum of methane combustion with its common radicals formed during combustion. The hydroxyl radical (OH*), as a main component in the chemical combustion process with its peak at 309 nm, starts forming at 1600 K and is observable during the main combustion process determining the flame front as well as after the main combustion [18,19]

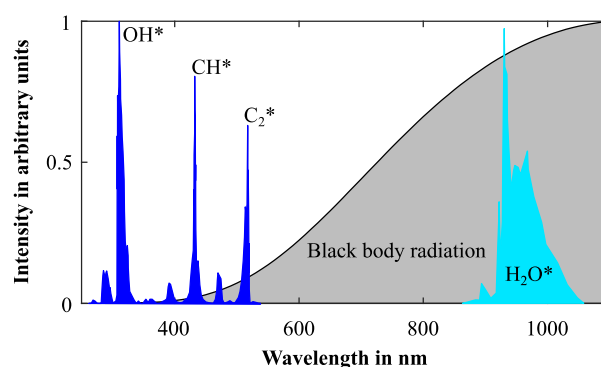


Figure 1. Intensity spectra of methane combustion (data taken from [20–22].)

To distinguish the flame front, the CH radical (CH^*), as an intermediate product of the hydrocarbon combustion to the final product CO_2 , is a further possible indicator. The CH^* mostly forms in regions with slight excess fuel and high temperatures. In addition, the CH^* consumption by the flame is faster than the one of OH^* and is responsible for the flame's blue color. Hence, the CH^* is also an indicator for the prompt NO-formation as the radical is bonding with the air's nitrogen to HCN and finally to NO ([18,20,23]).

The C_2 radical (C_2^*), with its peak at 517 nm, forms with a high concentration for premixed combustion under low air–fuel equivalence ratios. Further, C_2^* can act as a core for the polymerization of soot, thus presenting a first indicator for incomplete combustion. During combustion, the C_2^* radical radiates a large part of the combustion heat. C_2^* is responsible for flame colors ranging from yellow to green. ([18,19,24])

Further, background radiation originating from the broadband spectrum of CO_2^* (@340–650 nm), HCO^* (@340–523 nm) and HCHO^* (340–523 nm) (cp. [19,25]) exists, which is not included in Figure 1. Another major occurrence is the black body radiation from soot incandescence arising, e.g., from lube oil ignition, which partly overlays the combustion radical spectra. For the addition of hydrogen to the combustion of methane in a continuous burner [26], reduced global radical emission spectra can be observed, especially for the carbon-based radicals (CH^* , C_2^* , CO_2^*); this can be expected, as with an increased amount of hydrogen, the amount of methane decreases, and thus the amount of carbon atoms required to form these radicals diminishes. On the other hand, the global intensity of the OH^* radicals decreases despite the higher amount of hydrogen for the higher admixtures. This can be explained by the reduction of the CH^* radical, which reacts with O_2 and forms the hydroxyl radical.

Similar findings are presented in [27] for non-premixed combustion with an emphasis on the importance of CH^* radicals for OH^* radical formation. The more hydrogen admixture, the more the global emission spectra differ from the typical methane emission, with more H_2O radicals (H_2O^*) in the infrared region appearing due to an increasing amount of water (cf. [26]). Nevertheless, [20] mentions that this spectrum mainly arises from thermal excitation and less from chemical reactions. This was also observed in [7], especially after the combustion end was marked as 95% MFB. The H_2O^* radical is responsible for the red color of the flame.

Di Iorio [28,29] optically investigated the already mentioned increased laminar flame speed of higher hydrogen percentages using a Bowditch type (cp. [30]) passenger-car-size fully optical single-cylinder research engine. The flame front was detected through observations of the OH^* and CH^* radicals that were identified as flame front indicators.

As optical investigations of methane/hydrogen mixture combustion in large-bore applications are quite rare (cp. [7]), the following presents thermodynamical and optical measurement results of the combustion of NG, 5/95 and 10/90%_v hydrogen mixtures. The optical results are derived from the natural flame chemiluminescence captured with a new type of optical access.

2. Experimental Setup and Procedure

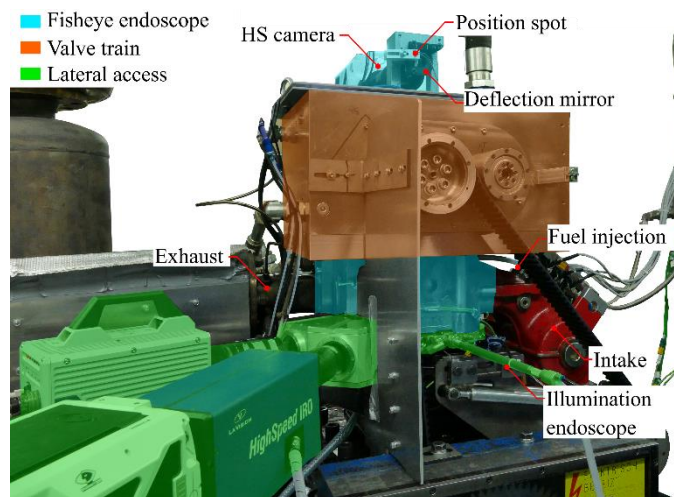
The test bench used in the following experiments is described in [7,31,32] and has already been used in different setups for other investigations. Therefore, the following sections only briefly summarize the main experimental setup and procedure.

2.1. Engine Setup

Table 2 summarizes the main dimensions of the test engine. The fully optically accessible engine consists of two access types—a lateral optical ring and a vertical fisheye endoscope, both shown in Figure 2. The lateral access is realized by inserting an intermediate ring between the cylinder head and the cylinder liner. It contains different mounting positions for an endoscope. For the following experiments, these positions were sealed with steel inserts, as no camera or illumination was used. The fisheye endoscope replaces an exhaust valve and realizes a view from the top.

Table 2. Engine properties.

Bore	170 mm
Stroke	210 mm
Connecting rod length	480 mm
Displacement	4.76 dm ³
Compression ratio	11.6
Ignition system	Unscavenged pre-chamber spark plug Spark plug
Engine speed	750 rpm
IMEP	16 bar

**Figure 2.** View of the engine setup at the test rig.

This top view is captured using a high-speed camera mounted outside of the engine to protect the camera from the engine oscillations, so the image is redirected by a 45° deflection mirror toward the camera. The camera is equipped with a Sigma macro-objective. The camera and the fisheye endoscope are aligned using a laser pointer mounted at the end of the endoscope, projecting the laser beam over the deflection mirror to the sigma objective. On the front of the objective, a blend can be mounted. Behind this blend, a mirror redirects the laser beam back to the laser pointer. The perfect alignment is reached as soon as the laser beam distinguishes and is not visible at the blend or the pointer itself. This proper alignment is especially important for the developed image post-processing algorithm mentioned in Section 4. The compensation of any relative motion between the camera and the fisheye endoscope, on the other hand, can be derived from the post-processing. As a reference point for this, a bright spot generated with an LED is rigidly fixed to the mirror frame.

The optically enhanced engine is capable of an extended skipped fire engine operation with at least a fired operation time of 74 s, resulting in 462.5 fired cycles at 750 rpm (cf. [33]). The description of the operation strategy as well as a comparison between the optical setup and the all-metal engine, can be found in [33]. A detailed description of the test bench design and its development can be found in [10].

2.2. Test Bench Infrastructure

The test bench features automated feeding of the preconditioned media for the cooling water, oil, air, gaseous, and liquid fuel. The natural gas was obtained from the municipal gas network. The gas mixtures are provided directly from the premixed gas bundles. The gas supply pressure is kept constant at 12 bar using a dome pressure regulator before supplying it to the engine's six gas injectors, three of each located at one inlet runner. The gas mass flow is measured using a Coriolis gas flow meter. The screw-type compressor is capable of supplying charged air up to 9 bar. The air mass flow is measured using

a rotary piston gas meter. To simulate a turbocharger pressure drop while upholding a constant turbocharger efficiency, a controllable flap is integrated into the exhaust path. A dynamometer is coupled with an induction machine to account for the high-power output of the single-cylinder engine. The test bench has an automated data acquisition system working with two different recording frequencies. The high-frequency resolution of 0.1 °CA captures the intake, exhaust, and combustion pressure. To record the combustion pressure, a Kistler 6041B piezoelectric pressure transducer and a 5011B charge amplifier are used. The intake pressure measurement uses a Kistler 4045A10 piezoelectric pressure transducer. The 4075A10 Kistler piezoelectric pressure transducer for the exhaust pressure measurement is coupled with a Kistler 7533B switching adapter to prevent the sensor from long-time exposure to high exhaust gas temperatures. The intake and exhaust pressure transducers are connected to a corresponding Kistler charge amplifier of type 4603 and plausibilized with a slow pressure measurement using a WIKA s10-type sensor. In addition to the automated data acquisition, an automated engine control system based on the National Instruments c-Rio and PIX system offers the possibility of both automated and manual control. An AVL Sesam FTIR conducts the measurement of exhaust species concentration. A description of measurement accuracy can be found in [33]. Those systems present state-of-the-art measurement techniques and equipment, and the measurements carried out show reproducible and small errors.

2.3. Fuel Properties

The experiments investigate the following fuel blends: 5/95, 10/90%_v Hydrogen/Methane and NG as reference fuels in comparison. These mixtures represent potential replacements for fossil natural gas in the natural gas grid infrastructure and are, therefore, relatively easily usable in the near future. Table 3 summarizes the properties of the municipal natural gas used. This mixture is assumed to be hydrogen-free, as the hydrogen concentration is below the detection limit.

Table 3. Properties of natural gas.

Methane Number	90	N₂ in %_v	0.2
Methane in %_v	95.7	Ethane %_v	3.2
CO₂ in %_v	0.7	Butane %_v	0.0695
Argon in %_v	0.1	H₂	-

Table 4 directly compares the fuel properties of the tested blends in contrast to the reference fuel, natural gas. The properties are derived from an experimental gas analysis conducted by a certified laboratory. The properties differ not much, so direct replacement seems possible.

Table 4. Properties of the used fuels.

	NG	5HCH₄	10HCH₄
H₂ in %_v	0	5	10
CH-ratio in -	0.25	0.243	0.236
ρ in kg/m³	0.657	0.653	0.649
H_u in MJ/kg	50.01	50.51	51.06
λ_{St}	17.23	17.35	17.49

2.4. Experimental Procedure and Settings

The investigations include a variation of the equivalence air–fuel ratio (λ) from 1.5 to 1.8 in steps of 0.1 with an increasing amount of air while keeping the amount of fuel constant. The equivalence air–fuel ratio is within an uncertainty of 0.23% resulting from the measurement devices. Further, the center of combustion (CoC), defined as a 50% amount of burnt fuel, varied in four discrete steps of $7 \pm 2^\circ$, $11 \pm 1^\circ$, $15 \pm 2^\circ$ and $20 \pm 2^\circ$ CA aFTDC

within the indicated limit throughout all equivalence air–fuel ratios. The adaption of the CoC results in an adaption of the spark timing. All variations are carried out for each fuel of Table 4 and for each ignition system with a common spark plug and an unscavenged pre-chamber spark plug. All investigations test a constant amount of fuel energy within a tolerance of 2%, necessitating an adjustment of the amount of fuel according to the extent of the hydrogen admixture. This results in an indicated mean effective pressure of up to 16 bar. Further, the geometric compression ratio of 11.6 was kept constant for all investigations.

The following thermodynamic results (burning duration, ignition delay, heat release rate, combustion temperature) are derived from a tuned GT-Power three pressure analysis (TPA) using the temperature results of 125 consecutive recorded engine cycles. Inputs for the calculation were the directly measured combustion chamber, inlet and exhaust pressures, which are averaged and corrected with a two-point offset. In the following presented burning duration, indicated efficiency, heat release rate and ignition delay are derived from the TPA. The CoV is derived directly from the measurement data using Equation (1) (cf. [34]).

$$CoV_{IMEP} = \frac{\sqrt{\frac{1}{N} \cdot \sum_{i=1}^N (IMEP_i - IMEP_m)^2}}{IMEP_m} \cdot 100\% \quad (1)$$

The indicated efficiency was calculated using direct measurements according to Equation (2).

$$\eta_i = \frac{0.5 \cdot n \cdot \oint p \cdot dV}{H_u \cdot \dot{m}_B} \cdot 100\% \quad (2)$$

For a detailed overview of the experimental setting, Table 5 summarizes the boundary conditions of the engine's media supply.

Table 5. Boundary conditions.

Air inlet temperature	45 °C
Gas inlet temperature	50 °C
Turbocharger emulator flap	Fully open
Cooling water inlet temperature	70 °C
Inlet pressure fuel gas	12 bar
Inlet oil temperature	80 °C

In contrast to [7,31,35], the herein presented investigations use the fully optically accessible engine and compare the combustion of an unscavenged pre-chamber spark plug to the combustion of a conventional spark plug using hydrogen methane blends and natural gas as a reference fuel. This first-of-its-kind optical investigation uses a fisheye optical system to observe these combustions. Further, the optical results are evaluated and compared to the thermodynamical findings.

3. Evaluation of Thermodynamic Results

The following sections summarize the thermodynamic results derived from the experiments to determine the effects of hydrogen admixture on the combustion process.

3.1. Burning Duration (MFB10-90)

The burning duration shown in Figure 3 is observed over a variation of the air–fuel equivalence ratio at a constant CoC of 8 °CA aFTDC (Figure 3a,b) and over a CoC variation at a constant air–fuel equivalence ratio of 1.7 (Figure 3c,d). The burning duration consists of the two timespans from the 10% mass fraction burned (MFB10) to 50% MFB (MFB50) and from 50% MFB to 90% MFB (MFB90). The division in these two parts shows the different influences of the admixture on the ignition and main combustion determined between the MFB10-50 and on the late combustion and burnout determined between MFB50-90. Regarding the ignition and main combustion, natural gas shows the longest

burning duration in both engine setups using the conventional spark plug (SP) and the unscavenged pre-chamber spark plug (UP-SP). The 10HCH₄ fuel mixture shows the lowest burning durations in both engine setups. Especially for high air–fuel equivalence ratios, the hydrogen admixture becomes more effective as the ignition and combustion conditions deteriorate. This improved lean burning behavior can be explained by taking the fuel properties of hydrogen into account, especially the improved ignition and laminar burning velocity (cf. [36]). Nevertheless, for lower air–fuel equivalence ratios, the influence of the hydrogen admixture on the combustion turns out to be smaller, as the ignition and combustion conditions are sufficient for both ignition systems used. Comparing both ignition systems, the unscavenged pre-chamber spark plug leads to a better ignition with a shorter burning duration and shows a greater impact of the hydrogen admixture at higher air–fuel equivalence ratios. Additionally, the unscavenged pre-chamber allows a stable engine operation with natural gas and 10HCH₄ at an air–fuel equivalence ratio of 1.8, whereas using the conventional spark plug leads to considerable misfiring and unstable conditions during the skipped fire engine operation and is, therefore, not shown. The main combustion recorded over a variation of the CoC at constant air–fuel equivalence ratio also depicts a reasonable behavior as the burning duration decreases for both ignition systems with earlier CoC, respectively, ignition timings. Furthermore, natural gas depicts the longest combustion and ignition durations for the conventional spark plug (cf. Figure 3c).

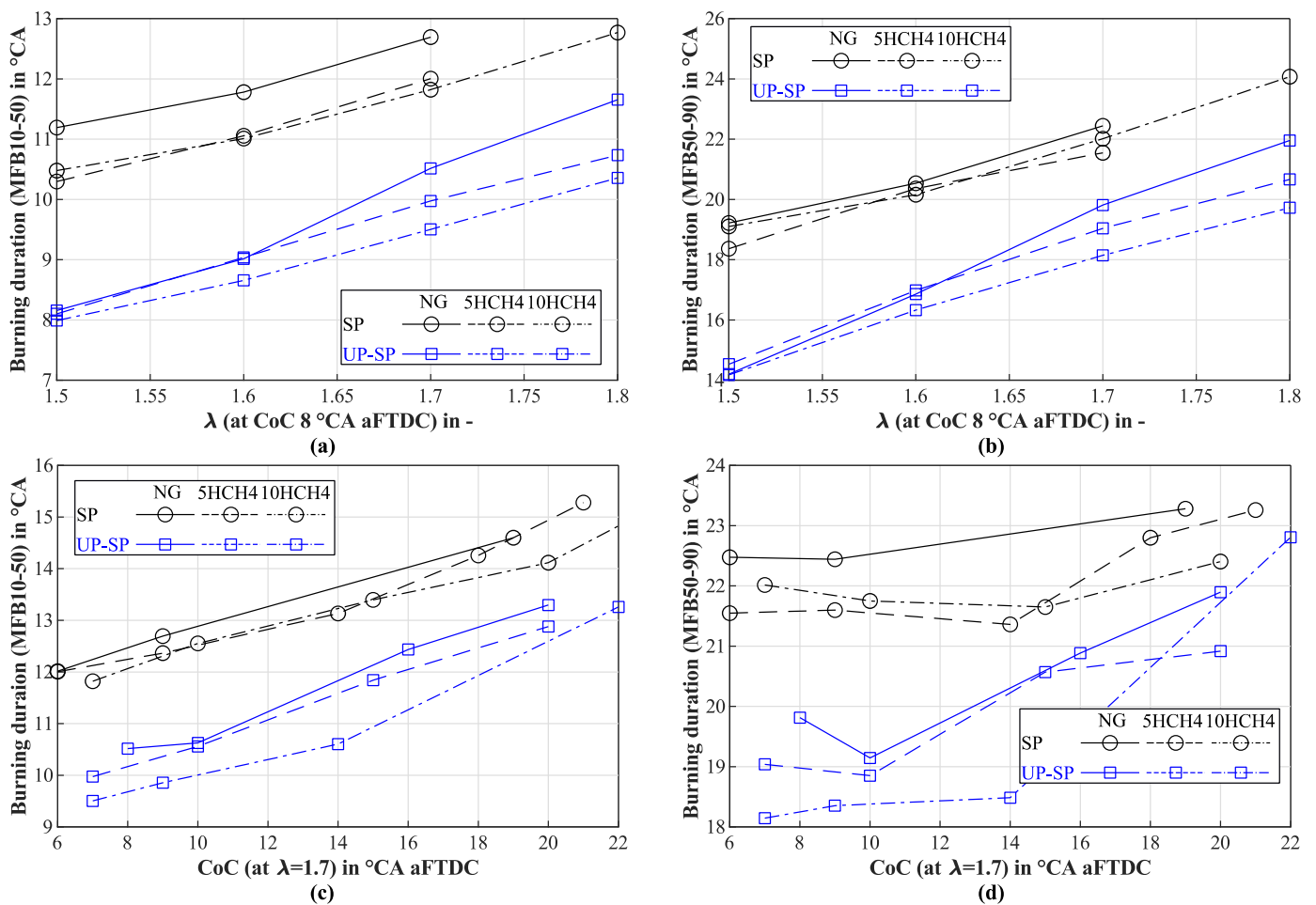


Figure 3. (a) Burning duration from 10–50 MFB at constant CoC = 8 °CA aFTDC; (b) Burning duration from 50–90 MFB at constant CoC = 8 °CA aFTDC; (c) Burning duration from 10–50 MFB at constant $\lambda = 1.7$; (d) Burning duration from 50–90 MFB at constant $\lambda = 1.7$.

The second stage of the combustion, which includes the burnout, shows a similar behavior as the main stage of the combustion for the air–fuel equivalence ratio variation (cf. Figure 3b). Increasing air–fuel equivalence ratios lead to elongated combustion durations as the laminar burning velocity decreases. Concerning the CoC variation, earlier ignition timings lead to earlier CoC, decreasing the burning duration. An increased influence is recognizable as the CoC is later than 15 °CA aFTDC. Nevertheless, the admixture of hydrogen improves the combustion of late CoCs as the laminar burning velocity is increased. This improves burnout and affects the emissions as well as the efficiency of the combustion.

3.2. Ignition Delay

The ignition delay shown in Figure 4 is calculated from the ignition timing until MFB2. It is obvious that the unscavenged pre-chamber spark plug reduces the ignition delay significantly, especially for higher air–fuel equivalence ratios. At the air–fuel equivalence ratio of 1.7, the difference between the ignition delay for NG is 18 °CA, for 5HCH₄ 11 °CA and 10HCH₄ 12.5 °CA. This is especially due to local air–fuel equivalence disturbances influencing the formation of a spark core in contrast to the unscavenged pre-chamber spark plug. In addition, due to the optimized design of the unscavenged pre-chamber's overflow bores, the turbulence in the pre-chamber can be increased to enhance the ignition and growth of the flame kernel (cf. [37]). Further, with increased air–fuel equivalence ratios, the local concentration of fuel near the conventional spark plug decreases, which deteriorates the initiation of the combustion as well as the propagation of the flame front starting at the conventional spark plug. The admixture of hydrogen especially supports the ignition using the conventional spark plug, whereas the effect of both hydrogen mixtures is almost equal. With the unscavenged pre-chamber spark plugs, the effect of the hydrogen addition is almost negligible for the here used amount and shows a clear improvement only at higher air–fuel equivalence ratios. Similar findings in [7] support the results.

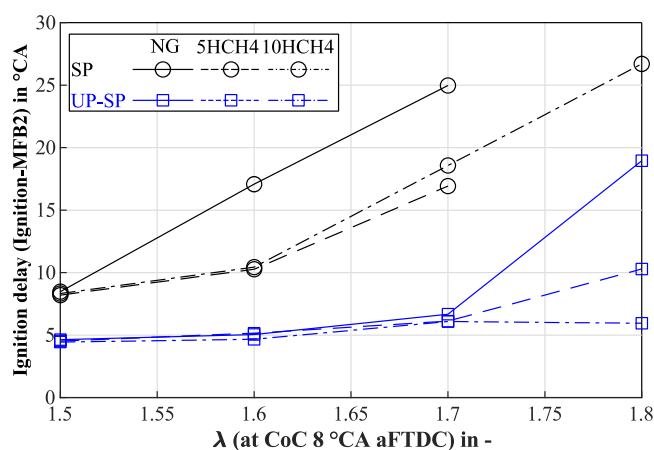


Figure 4. Ignition delay at constant CoC = 8 °CA aFTDC.

3.3. Coefficient of Variance (CoV)

Figure 5 shows the coefficient of variance (CoV) of the indicated mean effective pressure calculated according to Equation (1). Figure 5 also includes the stability limit of 2%, according to [38]. By covering a larger volume during ignition with the unscavenged pre-chamber, combustion runs more stable than using the conventional spark plug. With increasing air–fuel equivalence ratios, the combustion becomes more unstable as the cyclic variations increase until a misfire occurs. Especially for the conventional spark plug, this results in misfiring and, therefore, exceeds the stability limit. Even with the highest amount of hydrogen admixture used, here, the combustion using a conventional spark plug for ignition exceeds the stability limit at an air–fuel equivalence ratio of 1.8. The investigation results had to be neglected as severe misfires led to absolutely unstable conditions,

especially as the engine was operated under skipped fire operation. For the unscavenged pre-chamber spark plug, the admixture of hydrogen is much more beneficial and stabilizes the combustion, if only at higher air–fuel equivalence ratios, whereas at lower air–fuel equivalence ratios, almost no influence is visible. Further, the admixture is low enough that the effects of lube oil ignition cannot deteriorate the combustion stability, as experienced in [7], leading to abnormal combustion. Especially taking the skipped fire operation condition of the optical engine into account, the stabilization of the combustion with an increased admixture of hydrogen is beneficial, resulting in higher combustion temperatures, faster heat-up of the engine and, therefore, improved ignition and combustion conditions.

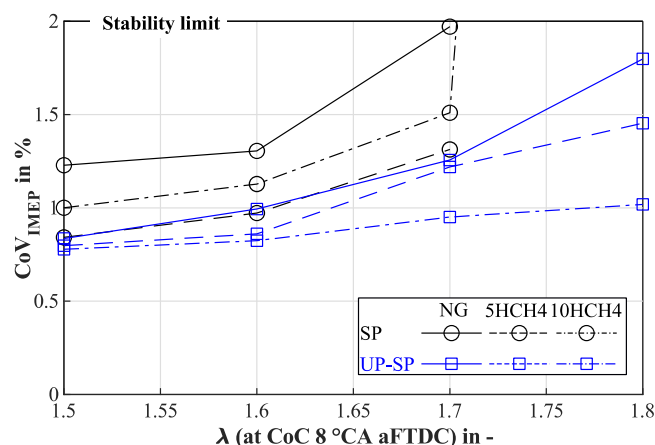


Figure 5. CoVIMEP at constant CoC = 8 °CA aFTDC.

3.4. Indicated Efficiency

Figure 6 includes the indicated efficiency at a constant CoC of 8 °CA aFTDC and at a constant air–fuel equivalence ratio of 1.7 each, with a variation in the air–fuel equivalence ratio, respectively, the CoC. The indicated efficiency was calculated using Equation (2) from filtered, corrected and averaged measurement data. The unscavenged pre-chamber spark plug shows higher indicated mean efficiency due to better ignition and, therefore, faster combustion for the air–fuel equivalence ratio as well as CoC variation. As the lean running limit is increased, this results in higher efficiency at higher air–fuel equivalence ratios for the unscavenged pre-chamber, whereas the spark plug is not capable of the ignition of lean mixtures resulting in misfires and decreased efficiency (cf. Figure 6a). Especially for higher air–fuel equivalence ratios, the benefit of hydrogen admixture is recognizable as the efficiency is increased compared to NG due to stable ignition and combustion. For lower air–fuel equivalence ratios, the effect is less decisive as the ignition conditions here are better compared to higher air–fuel equivalence ratios. Figure 6b shows the effect of the CoC influence on the indicated efficiency. With late CoCs, the efficiency of both ignition systems deteriorates as the combustion duration increases, leading to higher wall heat losses, exhaust gas temperatures and less usable heat for the pressure increase. Nevertheless, an admixture of hydrogen improves the indicated efficiency as it increases the laminar burning velocity of the fuel blend compared to NG.

3.5. Apparent Heat Release Rate (AHRR)

Figure 7 shows the heat release rate for both ignition systems and investigated fuels at a constant CoC of 8 °CA aFTDC and an air–fuel equivalence ratio of 1.7. Concerning the ignition system, the unscavenged pre-chamber shows later ignition timings due to a reduced ignition delay (cf. Figure 4) and reduced burning durations (cf. Figure 3).

The conventional spark plug needs much earlier ignition timings to overcome the deteriorated ignition behavior. Further, the addition of hydrogen only slightly alters the timing. The admixture results in a steeper heat release and higher peaks, as well as a retarded burnout. This supports the increased indicated efficiency of the combustion of

the fuel blends (cf. Figure 6). Compared to the unscavenged pre-chamber spark plugs, Figure 7b shows a much steeper and faster combustion with increased peak value and a further retarded burnout, resulting in an increased indicated efficiency. The addition of 2%V is only of less influence concerning the heat release, while the ignition delay of NG and 5HCH₄ are almost equal. Nevertheless, the peak value is 1.3 °CA earlier and 4.6% higher. The maximum hydrogen admixture shows the highest heat release peak, resulting in fast combustion.

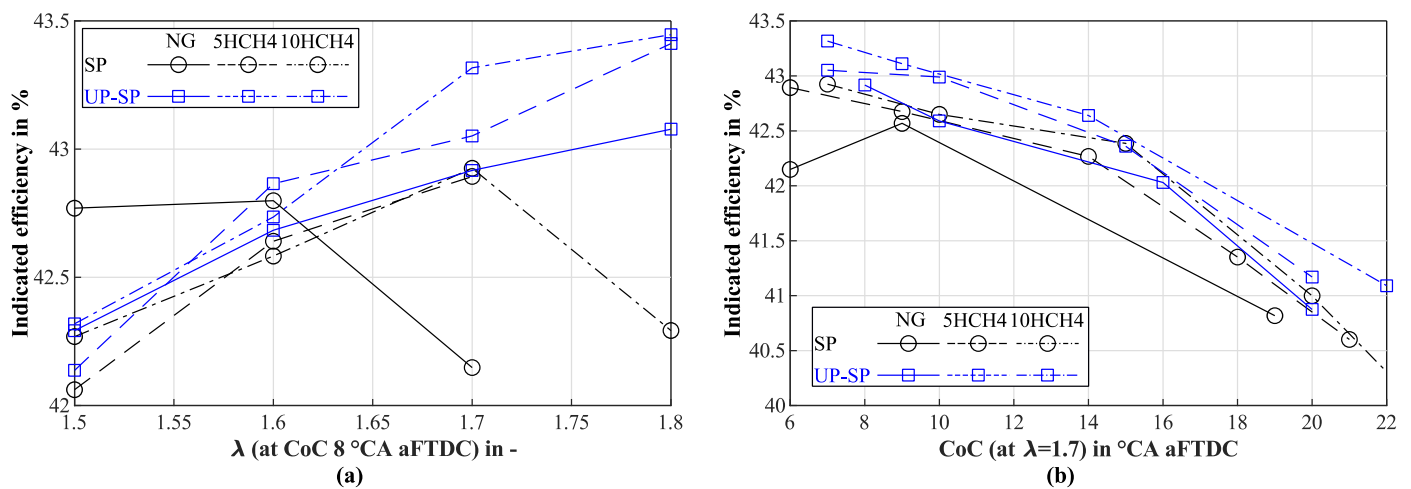


Figure 6. (a) Indicated efficiency at constant air–fuel equivalence ratio of 1.7; (b) Indicated efficiency at constant CoC of 8 °CA aFTDC.

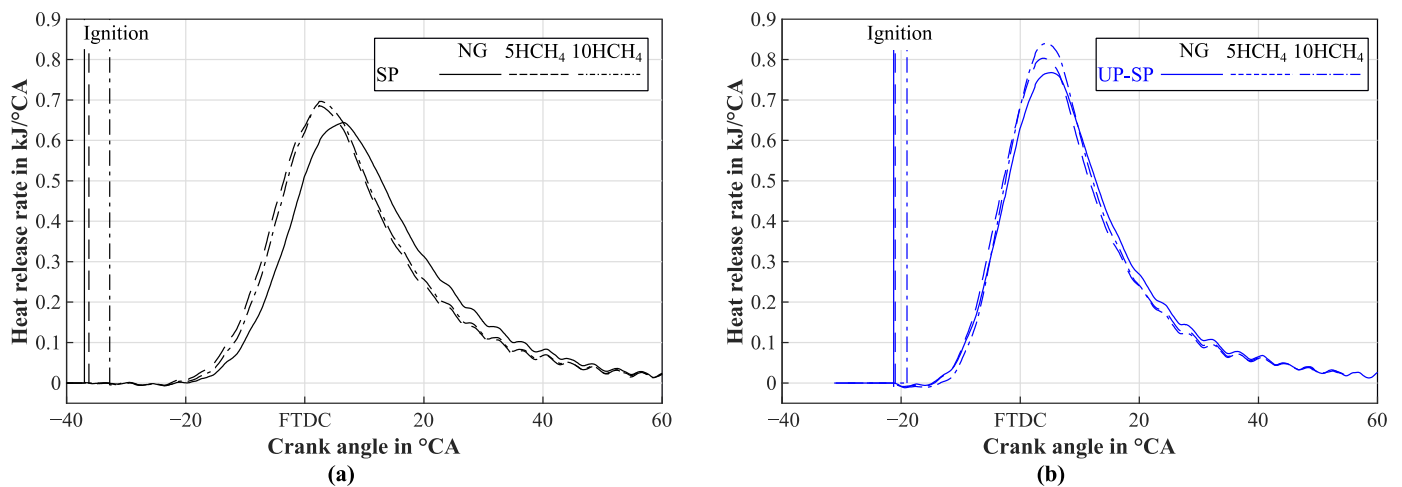


Figure 7. (a) Heat release rate for spark plug at CoC = 8 °CA aFTDC and air–fuel equivalence ratio 1.7; (b) Heat release rate for unscavenged spark plug at CoC = 8 °CA and air–fuel equivalence ratio 1.7.

4. Evaluation of the Optical Results

The optical investigations focus on intensity traces of the natural flame chemiluminescence to support the findings of the thermodynamically derived results. A comparison of images at specific points in the combustion cycle can be used to derive differences in the combustion between the two ignition systems and the different investigated fuels.

4.1. Procedure of the Image Evaluation

The pre- and post-processing follow the approach detailed in [35]. Figure 8 summarizes the preprocessing procedure implemented in Matlab. The preprocessing includes basic image arithmetic to rotate and mirror the image, the compensation of the image movement, a cutout of the ROI (region of interest) and a debayering to derive the colored images. The

post-processing includes the un-distortion of the images as well as a simplified reprojection algorithm detailed in Section 4.4. For this, a special calibration of the complete fisheye endoscope is necessary. The procedure behind the calibration is explained in detail in [35]. The calibration is carried out using the Kannala Brandt [39] approach. It is compared to an alternative approach in [35] and chosen as the most applicable. The calibration leads to the forward projection function shown in Figure 9, with a maximum angle of 97.2° and a maximum image radius of 203 px.

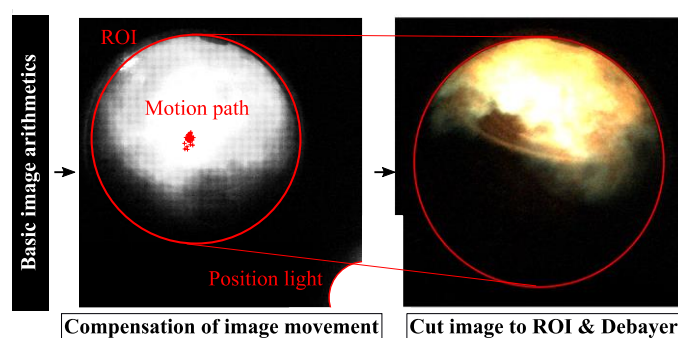


Figure 8. Preprocessing of images.

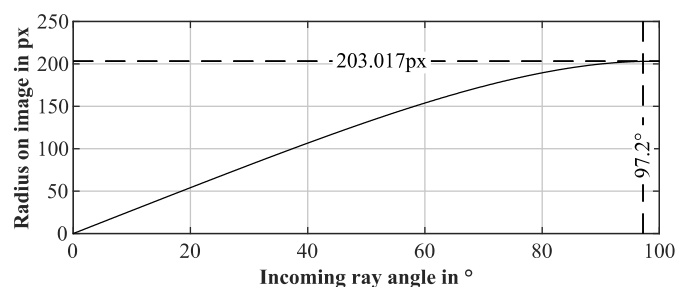


Figure 9. Forward Projection function derived from calibration.

The calibration for the imaging was carried out on a setup outside the engine with similar mounting conditions as at the engine (cf. Figure 10). The alignment of the camera towards the optic at the testing rig and at the calibration setup uses a laser beam extinction. The calibration setup outside the testing rig facilitates a homogenous illumination, as well as the usage of the calibration pattern with a size of $297 \text{ mm} \times 42 \text{ mm} \times 10 \text{ mm}$. The pattern consists of 17 columns and 12 rows, resulting in 204 regular black and white squares with 176 usable control points and 325 unique distances between them. To estimate the accuracy of the calibration, a reprojection of the calibration pattern to six different offsets from the first lens is carried out. For each reprojection, the algorithm shown in [35] was used to derive the visible distances between the control points. Figure 11 shows the standard deviation of the derived distance to the real one with 25 mm.

The quality of the results is dependent on the accuracy of the detection algorithm used to derive the control points from the image, the precision of the calibration itself and the accuracy of the measurement of the distance between the optic and the pattern. Especially due to the detection of the control points herein carried out with [40], the distance proves especially influential as its accuracy also determines the calibration quality. Further, the typical optical distortion effect of a fisheye optic can be seen in the results. With the object closer to the lens, the object becomes more distorted, resulting in a deteriorated resolution and, thus, a higher standard deviation. The higher standard deviation for the 24 mm distance results from the almost doubled amount of detectable and useable distances to determine the value. Here, the imaging results of the investigations can be used to derive a better estimation of the optic's accuracy. With an averaged standard deviation over all distances, a deviation of 3.3 mm compared to the engine's bore 2% proves a less comparable

deviation. A mean value over all investigated distances seems valid, as the observed natural chemiluminescence is an integral field of sight method.

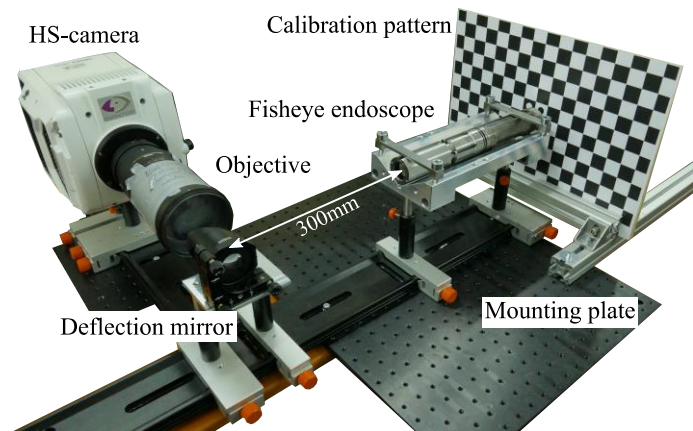


Figure 10. Calibration Setup.

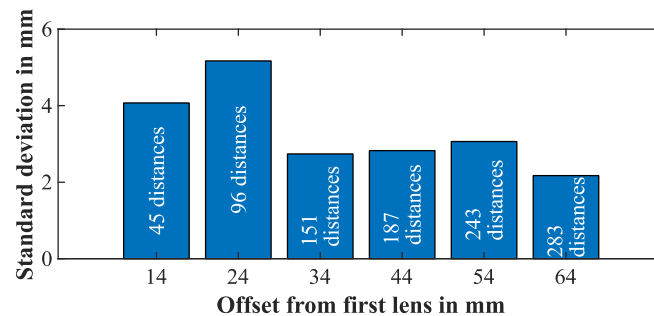


Figure 11. Standard deviation of distance between control points.

To further improve the accuracy of the reprojection algorithm, a tuning of the camera's position in the real world can be carried out if at least the real-world coordinates of one point in the image are known. Two visible control points in the image were used for this and compared to the digital mockup of the testing rig. The analysis showed a mean error of 3.2 mm for the reprojection and, thus, imaging accuracy.

4.2. Evaluation of the Natural Chemiluminescence Intensity Trace

Figure 12 shows the mean intensity trace over all recorded cycles for the CoC of 8, 10 and 15 °CA aFTDC and the different air–fuel equivalence ratios 1.5, 1.6, 1.7 and 1.8. Column 1 contains the traces for the unscavenged pre-chamber sparkplug, whereas column 2 shows the traces for the conventional spark plug. All traces are normalized relative to the maximum arising intensity for the unscavenged pre-chamber spark plug of CoC 8 °CA aFTDC and λ 1.5 to compare the intensity traces among the different CoC and air–fuel equivalence ratios as well as for both ignition systems. As already shown in the evaluation of the thermodynamic results, it is not capable of a stable ignition, respectively, combustion for the air–fuel equivalence ratio of 1.8, so no characteristic behavior can be determined. Thus, they are not included in the optical evaluation. According to Figure 12, a postponed center of combustion results in a less intense natural flame chemiluminescence. This can be explained by a reduced combustion temperature, resulting in a less intense broadband luminosity of the combustion.

The comparison of the combustion temperature derived from the TPA model with the intensity for the unscavenged pre-chamber spark plug at λ 1.5 and 1.8 for 10HCH₄ and NG under the CoC variation is shown in Figure 13. Here, the decrease in the combustion temperature with higher air–fuel equivalence ratios as well as with late CoCs is visible. In

particular, for the CoC of 15 °CA aFTDC, the maximum occurring temperature is retarded for all air–fuel equivalence ratios. This results from delayed and slow combustion under these conditions.

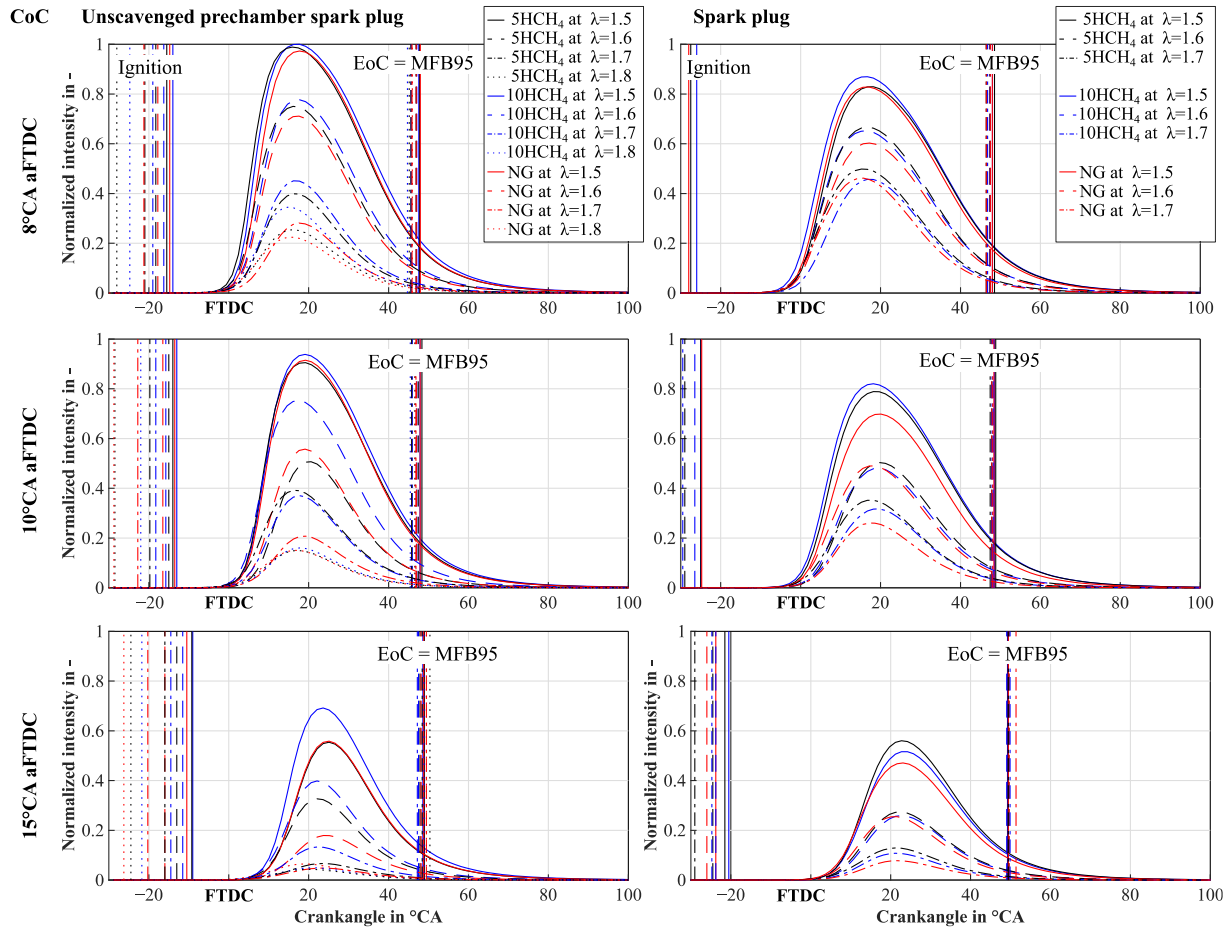


Figure 12. Intensity trace of the natural chemiluminescence for a CoC and air–fuel equivalence ratio variation comparing an unscavenged pre-chamber sparkplug to a spark plug.

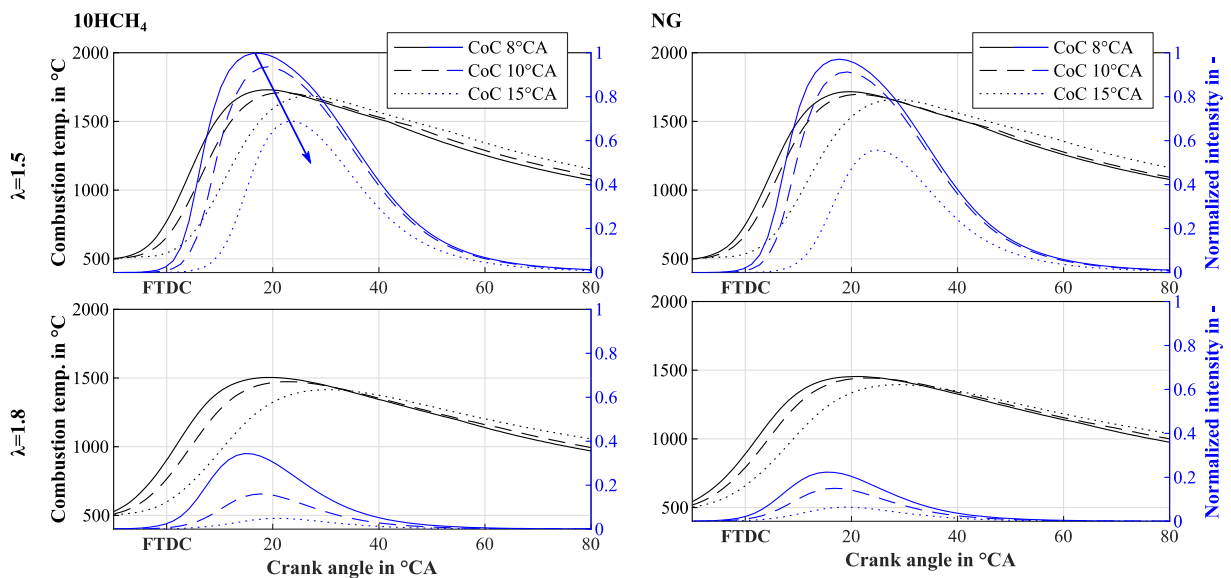


Figure 13. Normalized intensity traces and combustion temperatures for CoC variation at $\lambda = 1.5$ and 1.7 for the unscavenged pre-chamber spark plug.

Further, the conditions for the chain branching mechanism of the combustion deteriorate towards lower pressure and temperature during the combustion for late CoCs. This behavior is observable for both ignition systems, and an even lower intensity can be observed for the conventional spark plug due to a lower ignition performance, leading to an even more deteriorated combustion for later CoCs. The behavior of the air–fuel equivalence ratio variation seems valid, taking higher combustion temperatures (cf. Figure 13) and faster combustion into account. The higher combustion temperature arises from lower air–fuel equivalence ratio values due to a higher amount of fuel and less surplus air. In addition, a higher broadband luminosity from less quenching between the excited combustion molecules with oxygen for lower air–fuel equivalence ratios results in higher intensity (cf. [41,42]). The faster combustion leads to an early generation of chemiluminescence arising from carbon-based radicals with higher energy content, resulting in more intense radiation. This can be observed in Figure 13, as for low air–fuel ratios and early CoCs, the intensity's maximum is within 1 °CA difference between the temperature and intensity trace. For late CoCs, the combustion slows down, and the offset between the temperature and the intensity increases to almost 3 °CA. This becomes even more for high air–fuel equivalence ratios, as quenching and a further decrease in burning velocity occur. A difference of 10 °CA develops between the two maxima. The behavior between the maximum admixture of 10%_V hydrogen and the NG is similar.

For the unscavenged pre-chamber spark plugs, the 10%_V hydrogen admixture shows the highest natural flame chemiluminescence intensity due to the highest combustion temperature (cf. Figure 13) with the most broadband radiation. This difference becomes more obvious as the ignition and combustion conditions deteriorate for a higher air–fuel equivalence ratio and a later CoC. The increased amount of hydrogen in the mixture counteracts the deteriorated conditions for ignition and combustion. Especially for the lowest air–fuel equivalence ratio of 1.5 and the earliest CoC of 8 °CA aFTDC, the difference between the fuel mixtures and the reference fuel NG is quite small. The same behavior can be observed in Figure 13 when comparing NG and 10HCH₄ at λ 1.5. The combustion temperatures are quite equal, with a difference of 40 °C for the earliest CoC and also for the CoC 10 °CA aFTDC. With the late CoC 15 °CA aFTDC, the influence becomes remarkable. This is due to the optimal ignition conditions at early CoC, a low air–fuel equivalence ratio and stable and complete combustion, resulting in high combustion temperatures and, thus, the high intensities of the broadband radiation. Those operating points are also quite similar because of the limited resolution of the camera, as all images are captured with the same exposure time for comparability. Nevertheless, as already shown in section three, the unscavenged pre-chamber spark plug shows a stable ignition, even for the deteriorated conditions at late CoC and high air–fuel equivalence ratios, and all used fuel mixtures. The results show similar behavior as mentioned in [7]. However, the end of combustion marked as MFB95 cannot be correlated with the natural chemiluminescence as further intensity above the MFB95 is visible. Similarly to what was discussed in [7], this can result from excited water forming during the after-combustion phase. Especially with a higher content of hydrogen and a lower air–fuel equivalence ratio, the intensity after the end of combustion is higher, resulting from higher combustion temperatures.

The offset of the CoC and the center of intensity (CoI) shows a mean value of 13.98 °CA and a standard deviation of 2.2 °CA for the unscavenged pre-chamber spark plug. The offset between the CoC and CoI for the conventional spark plug shows a mean value of 14.29 °CA and a standard deviation of 2.2 °CA. The difference between the CoI and the CoC of both ignition systems for all the investigated variations seems almost constant with at least 14 °CA.

4.3. Evaluation of Combustion Image Series

Figure 14 shows the combustion image series for the MFB5, MFB10, MFB50 and MFB95 at 8° CoC and an air–fuel equivalence ratio of 1.5 and 1.7 for the unscavenged pre-chamber spark plug for NG and a 10%_V admixture of hydrogen. The image intensities

are scaled individually for each MFB for better visibility but are constant for the different fuels. The images are taken from the 25th recorded cycle out of 50 and are not depicting the mean value.

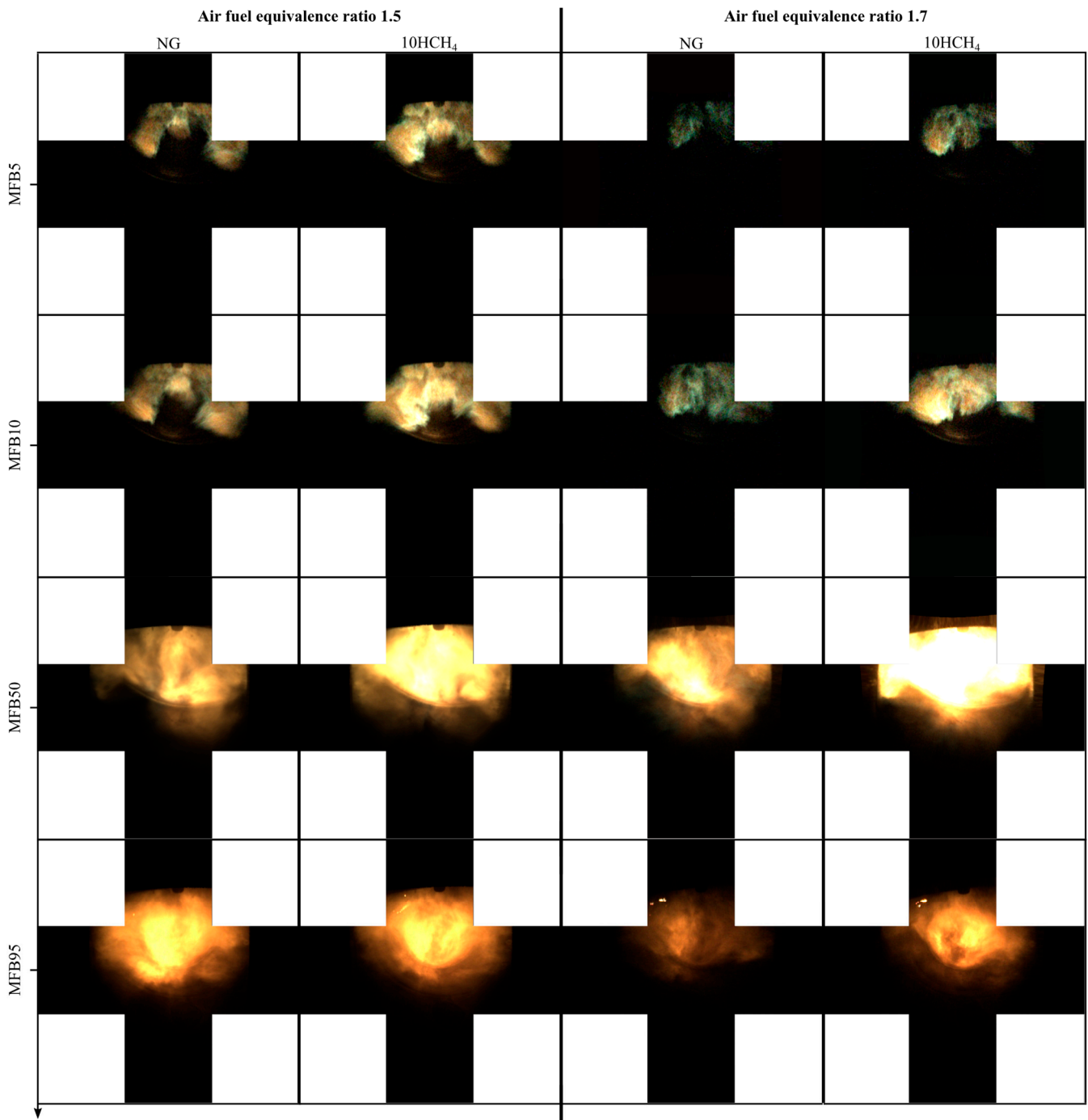


Figure 14. Combustion image series for MFB5, 10, 50 and 95 for the unscavenged pre-chamber spark plug at 8° CoC and air–fuel equivalence ratio of 1.5 and 1.7.

Further, the images are dewarped using five different pinhole projections (cf. [35]), resulting in the specific display format. Figure 15 shows the same arrangement for the conventional spark plug. As already described in Section 1, the radicals arising during combustion are responsible for the flame’s color. A comparison of the two fuels for the respective air–fuel equivalence ratio shows only a few differences in the color composition of the flame for both ignition systems. For the air–fuel equivalence ratio of 1.5 using

the unscavenged pre-chamber spark plug (cf. Figure 14), only the early stages of the combustion of NG and 10HCH₄ at points MFB5 and MFB10 show blue areas at the flame front. These can be attributed to the formation of CH* in the outer edges of the flame, the reactive flame front. In the early stages of the combustion of 10HCH₄, some yellow areas can already be seen in the flame, which can indicate higher combustion temperatures as well as faster combustion leading to the earlier formation of more C₂*.

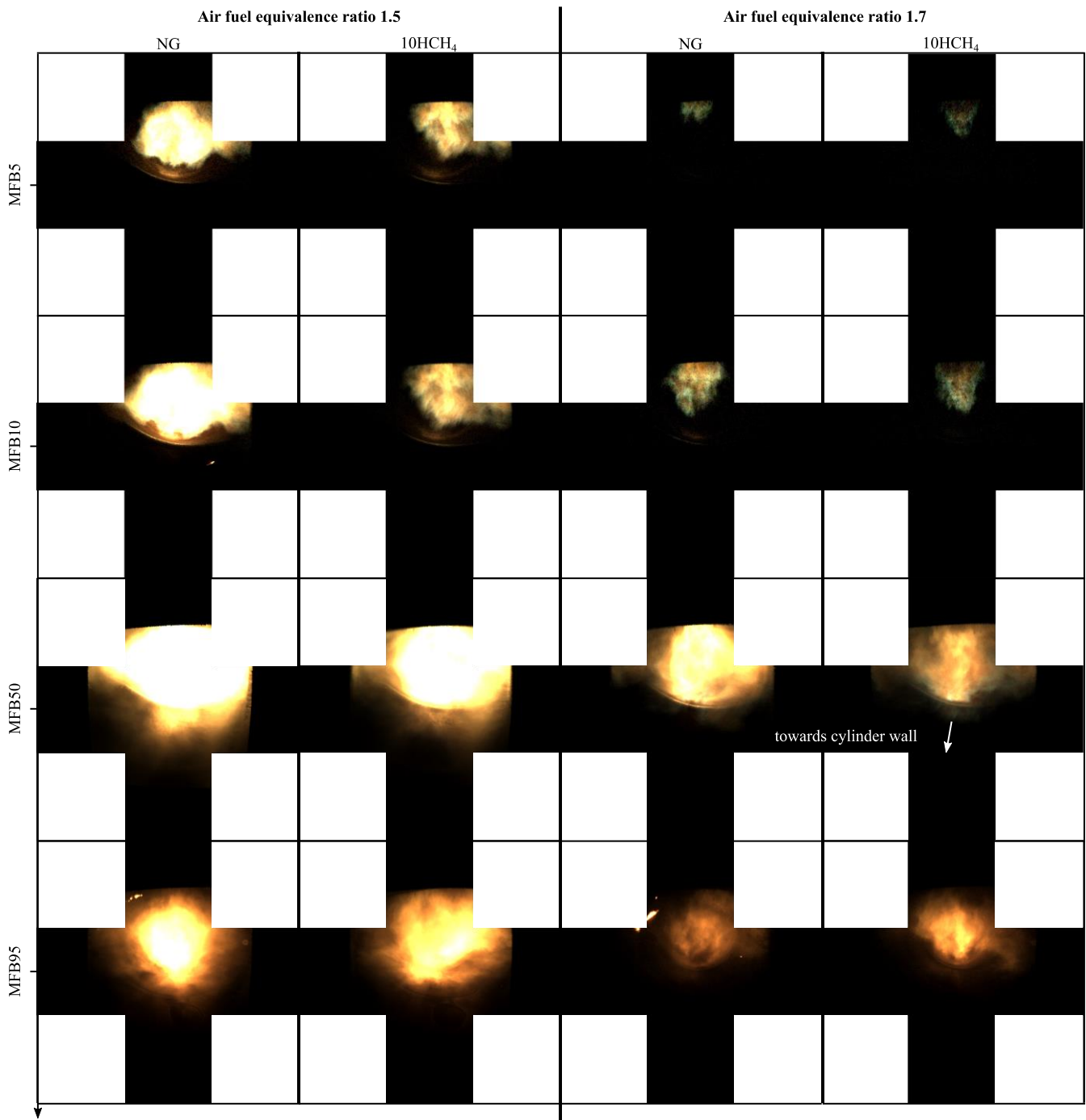


Figure 15. Combustion image series for MFB5, 10, 50 and 95 for the conventional spark plug at 8° CoC and air–fuel equivalence ratio of 1.5 and 1.7.

With MFB5, both flames show a reddish portion, which can be an indicator of the formation of water. The center of combustion shows a strong yellow flame, indicating

a high combustion temperature and the resulting strong black body radiation and C_2^* formation. Further, there are reddish areas at the boundaries of the deep yellow parts of the flame. This intensifies as the flame progresses toward the burnout phase and is clearly visible for MFB95. Here, a bright yellow core is now formed, blending into the red spectral range in the direction of the combustion chamber wall.

At the air–fuel equivalence ratio of 1.7, a clearly more pronounced blue component for the combustion of natural gas in the early stages of combustion compared to the mixture with 10%_v hydrogen is visible. Due to the lower combustion temperatures in areas of leaner λ , a lower temperature-dependent background radiation, as well as a lower production of C_2^* , is to be expected. Nevertheless, the flame with a higher hydrogen content and thus a higher combustion temperature already shows first reddish (MFB5) and then first yellow (MFB10) areas. Further, these are due to the stronger black-body radiation of burning carbon at higher combustion temperatures at MFB50. During the burnout phase and the end of combustion (MFB95), shifted portions of the flame can also be seen in the direction of the combustion chamber wall as well as in the center, colored in the red spectral range, which could be attributed to the formation of thermally excited H_2O^* .

A comparison of the two λ shows a clearly higher blue portion of the color for higher oxygen content, at least for the early phases of the combustion caused by the CH^* that is well visible because of the lower superimposed background radiation and a slower combustion velocity. At the end of combustion and during the burnout phase, the images with a leaner air–fuel equivalence ratio show a slightly more pronounced shift into the reddish range. This is also resulting from weaker background radiation and lower temperatures during the burnout resulting from an overall lower combustion temperature.

For the conventional spark plug test series (cf. Figure 15), an almost similar behavior can be observed. For low air–fuel equivalence ratios, blue parts in the flame front at the early stage of combustion hint at CH^* formation. At an air–fuel equivalence ratio of 1.7, the images show a slight blue part at the edges of the flame at CoC, which is propagating toward the combustion chamber wall. These are visible as the combustion temperature is lower compared to the experiments using the unscavenged pre-chamber spark plug and, therefore, is less concealed by background radiation. Further, the slower combustion for high air–fuel ratios and the conventional spark plug results in a delay in the radical formation. The higher intensities displayed for the natural gas compared to the 10HCH₄ combustion at an air–fuel equivalence ratio of 1.5 arise from the cyclic variations.

Comparing the images of the unscavenged pre-chamber spark plug and the conventional spark plug in Figures 14 and 15, a different flame propagation is visible. Especially in the early stage of the combustion, the areas ignited by the torch flames are visible in Figure 14, whereas Figure 15 shows a more compact area of the flame for the conventional-spark-plug-ignited combustion.

4.4. Evaluation of Torch Rays

For the unscavenged pre-chamber spark plug, a closer look at the early stages of the combustion shows the formation of torch flames originating from the unscavenged pre-chamber spark plug combining to create a continuous flame front (cf. Figure 16). Due to the position of the fisheye optical system, not all of the unscavenged pre-chamber spark plug's torch flames are visible in the recordings, as the rest is covered by the cap of the ignition system itself. Figure 16 shows the recorded image series for the 10HCH₄ fuel at CoC 8 °CA aFTDC with an air–fuel equivalence ratio of 1.7. The images depicted are mean-value images over the 50 recorded cycles. The image recognition results of the detection algorithm used to extract the four visible torch flames out of a total of seven are included in Figure 16. The torch flames all have a bluish color indicating a quite high concentration of CH^* responsible for the flame's blue color that is overlaid with yellow and orange, hinting at carbon-based radiation as the °CA advances. Figure 17 shows the arrangement of the torch flames. The algorithm for extracting the torch flame contour stops when a

continuous bright flame front forms. Since not all torch flames can be detected equally well, the following evaluation concentrates on the one pointing downward with the number 7.

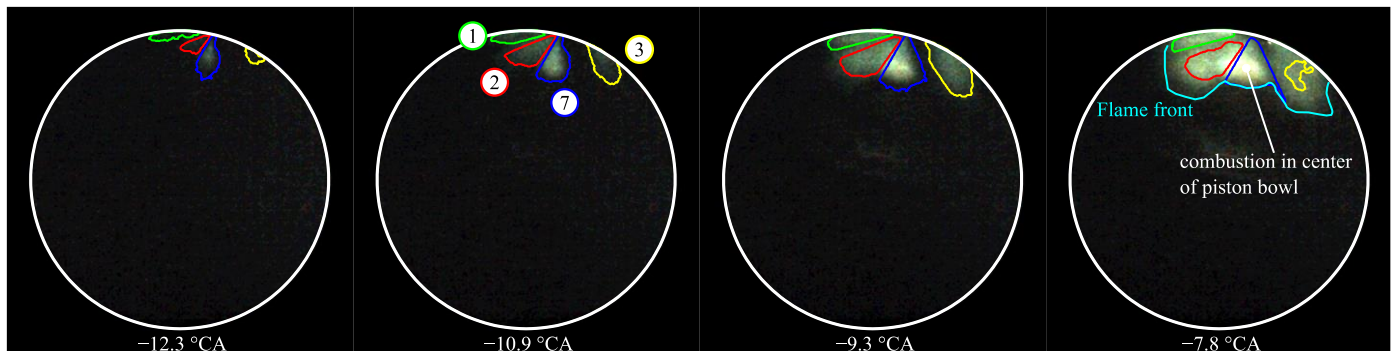


Figure 16. Image series of torch ray of 10HCH₄ at CoC = 8 °CA AFTDC and $\lambda = 1.7$ (numbers indicate torch ray).

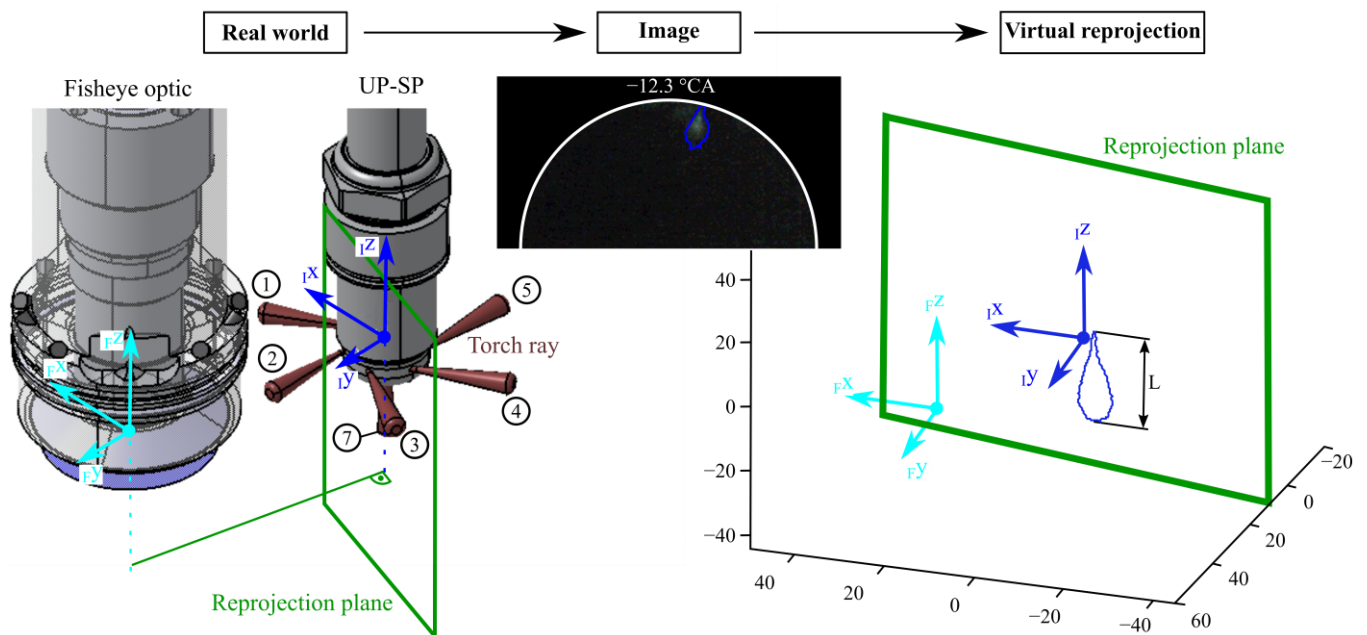


Figure 17. Proceeding of virtual reprojecting to derive the torch ray length L using the visible natural chemiluminescence (numbers indicate the different torch rays).

It has the shortest distance to the piston bowl and even extends as far as the bowl itself, as will be shown in Figures 18 and 19. Figure 17 shows the detailed proceeding for the reprojecting post-processing, which is similar to the one presented in [35]. The reprojecting plane used for the post-processing is perpendicular to the connection vector of the orthogonal projection points of the camera and ignition system origins to the horizontal base plane. After the virtual reprojecting, the length of the torch flame L can be derived from the post-processed images. This is undertaken for both fuels of NG and 10HCH₄ at the CoC of 8 °CA aFTDC and air–fuel equivalence ratios of 1.5, 1.6 and 1.7. Figures 18 and 19 summarize the results. Both figures show the mean value images of the 50 recorded cycles and are dewarped and individually scaled regarding their intensities for better visibility. Each figure contains the derived torch flame length, L , estimated as the max distance of the torch flames flame front to the engine’s flame deck (cf. Figure 18). Further, three different points on the piston bowl’s omega shape are overlaid to verify the length of L in accordance with the piston position over the engine rotation (s1–s3 cf. Figure 18).

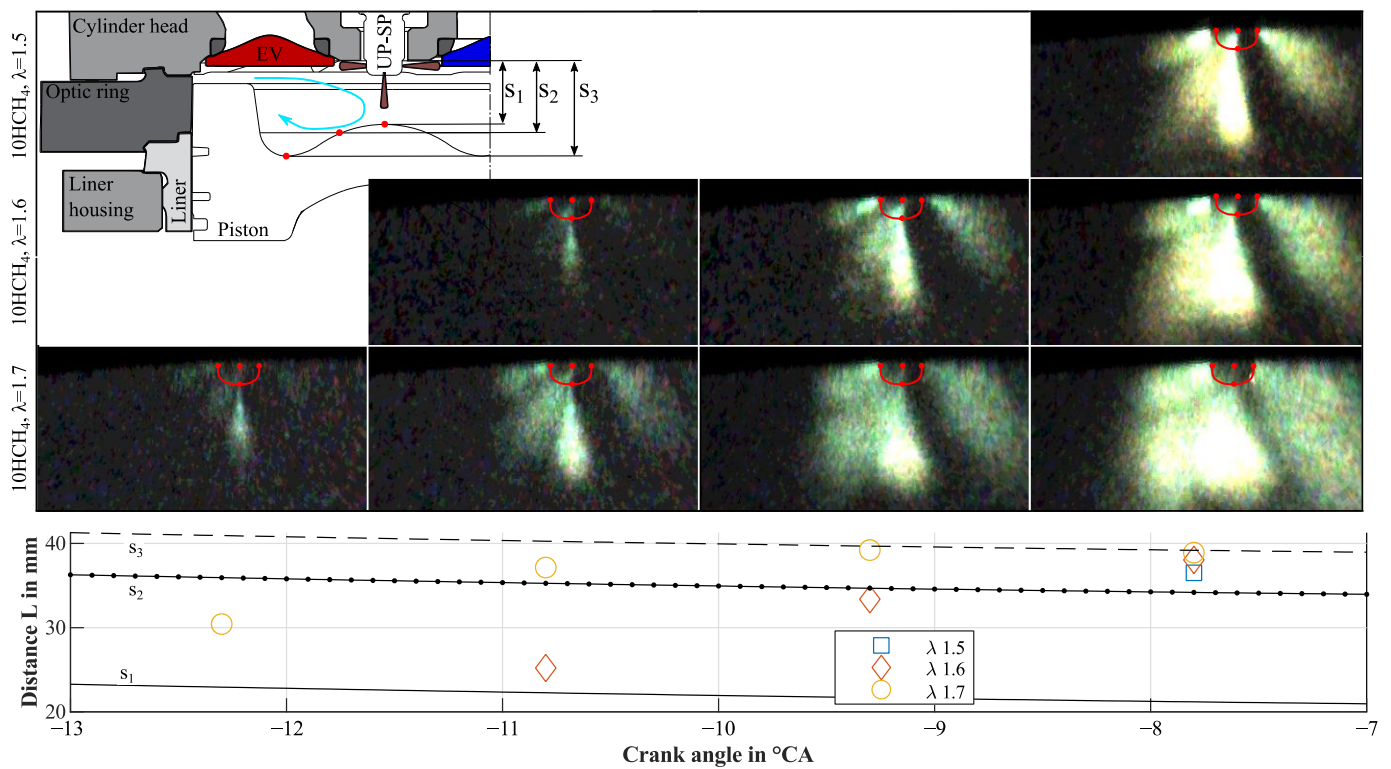


Figure 18. Torch ray images for $10HCH_4$ at $CoC = 8^\circ CA$ AFTDC and $\lambda = 1.5, 1.6, 1.7$. Distances s measured from the flame deck to the piston bowl.

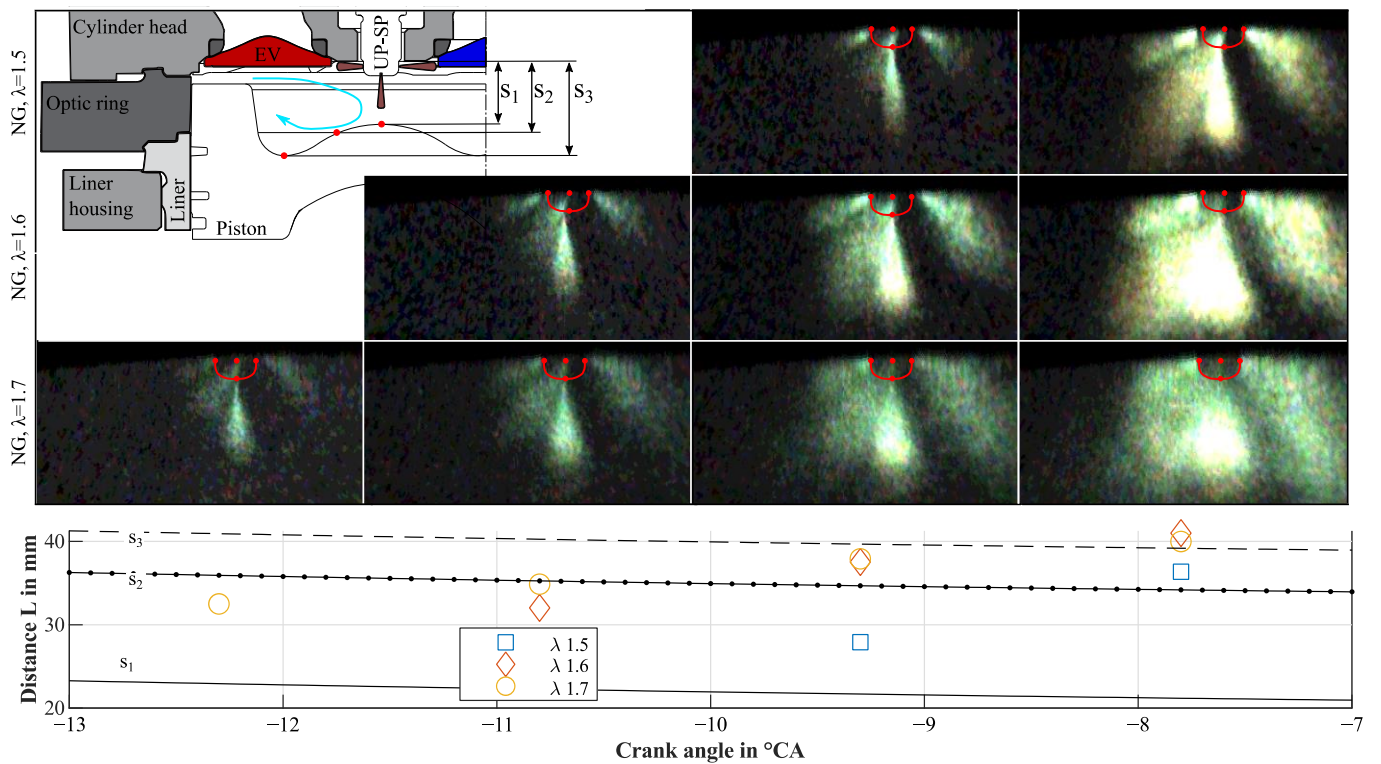


Figure 19. Torch ray images for NG at $CoC = 8^\circ CA$ AFTDC and $\lambda=1.5, 1.6, 1.7$. Distances s measured from the flame deck to the piston bowl.

Comparing the derived length of L with these distances, it becomes evident that the detected torch flame is being redirected within the piston bowl. The tip of the torch flame

touches the highest point of the piston at s_1 even before the images are captured, as the derived length is always larger than s_1 . Due to the omega-shaped piston bowl and the squish flow, the flame is redirected towards the lowest point of the piston shape marked as s_3 . This can be recorded as the used measurement technique is an integral line of sight method, which captures all the intensity along a line of sight. Especially for the highest air–fuel equivalence ratio resulting in the slowest combustion, the development of the torch flame and the interaction of flame number 7 with the piston bowl can be seen for both fuels. The tip of flame 7 is growing stronger perpendicularly to the flame axis and shows a higher intensity as here, a larger volume already ignites and contributes to the captured intensity. The first part of flame torch 7, at about one-third from its origin, is very narrow and compact, hinting at a high flame velocity and momentum at the exit of the unscavenged pre-chamber. The other three visible torch flames are difficult to distinguish from the background noise. During combustion, the horizontally aligned torch flames progress along the jet axis, but mainly perpendicular to it, so that the combustion chamber formed by the cylinder head and piston bowl is covered increasingly by the flames. This can be explained, among others, by the swirl and squish flow of the engine as well as by the mounting position of the unscavenged pre-chamber spark plug. The mounting position prevents the horizontally aligned torch flames from propagating too deep into the combustion chamber in the direction of the torch flame axis as their paths intersect partially with the engine's valves. For lower air–fuel equivalence ratios, the combustion progress is so fast that only a few pictures can be captured. Here, the torch rays also develop more quickly and show bright combustion that is already turning yellow, implying a later stage of combustion and C_2^* -based chemiluminescence with a higher intensity. The MFB5 is identified to occur after the flame torches form a continuous flame front and at crank angles later than the depicted 7°CA bFTDC . The detected length, L , of torch flame 7 is of a quite similar length for both fuels, as the torch flame reaches the piston bowl and is thus limited to the maximum possible length s_3 within the algorithm's reprojection accuracy (cf. Section 4.1). The mean images of the torch flame of both fuels also show quite similar intensities and very similar colors. This may be due to the comparable low admixture of hydrogen with only 10%_v. As also observed in [43], the 10%_v admixture shows a modest increase in the laminar burning velocity.

5. Summary and Discussion

5.1. Thermodynamic Results

The thermodynamic results all show plausible and explainable behavior that is also comparable to the combustion within an all-metal engine, as shown in [33]. This means that the setup is capable of a sufficient fired run time to stabilize the combustion and record the measurement data. The skipped fire operation mode even benefits from the admixture of hydrogen by a faster heat up of the combustion chamber and a faster stabilization but it also increases the thermal load onto the optical components. The herein investigated two different volume percentages of hydrogen cause no abnormal combustion and are, therefore, suitable for the engine by solely adapting the spark timing.

The results of the test series show that even with a small amount of hydrogen admixture, the combustion process gains higher efficiency and combustion stability because of the enhanced lean running limit. This is especially true for the setup with a conventional spark plug but is also beneficial for the unscavenged pre-chamber spark plug. Here, the combination with the admixture of hydrogen enhances the lean running limit further as the ignition and combustion benefit from the higher laminar burning velocity of the hydrogen. With the elongation of the lean running limit, a NO_x equivalent running strategy seems possible (cf. [7]) despite the higher combustion temperatures arising from the admixture of hydrogen that increase the NO_x concentration.

5.2. Optical Results

The imaging was conducted using a fisheye optical system that was mounted in the cylinder head. Due to the integration of the optic into the engine using a non-central mount a large part of the extensive field of view is not usable. Regarding optical quality, the optic is capable of images with a resolution of 1.5°CA , resulting in $330\ \mu\text{s}$ gate time. With this setting, a sufficient intensity and usable field of view are possible to even capture the early stage of the combustion, especially for the unscavenged pre-chamber spark plug.

Compared to the spectrometer investigations of premixed methane and blended methane/hydrogen combustion in a continuous burner presented in [26,44], the admixture of 10%_V hydrogen has no significant influence on the combustion spectra intensities. Therefore, the assumption of a similar spectrum of the methane and fuel blend combustion seems feasible. Further, [45] show the influence of the air–fuel equivalence ratio and the admixture of hydrogen on the flame emission. With high air–fuel equivalence ratios for natural gas flames, the intensity of the CH^* (@431 nm) decreases, whereas the emission of the C_2^* (@516 nm) radical vanishes, which is also responsible for the yellow part of the flame. The recorded natural chemiluminescence intensities seem, therefore, mainly dominated by the air–fuel equivalence ratio (cf. traces in Section 4.2 and combustion images in Section 4.3). This results in strong intensities from background radiation at low air–fuel equivalence ratios and overlays the much weaker intensities of the intermediate species, e.g., CH^* , which is formed mostly in the reactive flame front. Further, the higher burning velocity supports a faster conversion of the fuel and thus offers less time for the intermediate radical's radiation.

The presented intensities traces (cf. Section 4.2) of the natural flame chemiluminescence show a clear difference between the unscavenged pre-chamber spark plug and the conventional spark plug and some slight changes between the NG and the highest tested amount of hydrogen admixture of 10%_V. A higher intensity of the natural flame chemiluminescence for hydrogen admixtures hints at combustion with higher temperatures and, thus, assuming the same energy content for all tests, proves the combustion to be more efficient. Further, a faster increase in the intensity traces leads to a faster combustion, resulting in a faster heat release.

The Interpretation of the flame color uses dewarped images and supports the temperature, respectively, air–fuel equivalence ratio dominated intensities, as well as the findings from [26,44,45]. With colder combustion temperatures at high air–fuel equivalence ratios and a slower combustion, a more blue part of the flame is visible and less overlaid by background radiation as well as the more intense C_2^* radical vanishes at high air–fuel equivalence ratios (cf. [45]).

For the investigation of the torch flame, dewarped mean value images and the presented reprojection algorithm are used.

The virtual reprojection method is used to have a first look at the torch flame development using mean value images of the early stage of the combustion with the unscavenged pre-chamber spark plug. The used virtual reprojection underlies simplifications assumption and inaccuracies such as:

- The contour extraction uses predefined sectors for each torch flame and a global threshold in each sector for image binarization. The threshold is optimized to reduce the standard deviation of the extracted contour over the different thresholds.
- The reprojection is dependent on the accuracy of the optic's calibration.
- Due to the used integral line of sight method used here, intersecting or overlaid intensities lie in the same line of sight and cannot be distinguished. This deteriorates the accuracy of the torch flame recognition and thus decreases the quality of the virtual reprojection compared to laser-based investigations using specific and determined sheets for observation.
- As the engine uses a swirl in the charge air movement and the torch flame number seven is aligned with the cylinder bore axis, the influence arising from the swirl onto the torch flame is almost negligible.

- As natural chemiluminescence images are used, it is not possible to distinguish between the combustion radicals.
- The usable signal noise ratio is low for the detection of the torch flame.

Nevertheless, the virtual reprojection is a simple method to have the first easy-to-use comparison of the carried out natural chemiluminescence measurements to characterize the observed combustion. Further, the method can be used in case of a comparison with CFD results by deriving the same views with the same herein-used projection method.

Korb [46] presents different ignition regimes of a scavenged pre-chamber for different holes of the pre-chamber as well as different cycles. Xu [47] presents time-resolved optical investigations of the natural OH* radical chemiluminescence in an RCEM for an unscavenged pre-chamber spark plug igniting natural gas. Due to a missing lift-off length of the observed ignition, the combustion is flame based. The RCEM used in these experiments shows interference of the torch flame oriented parallel to the cylinder axis with the piston.

The presented investigation uses mean value images to derive the torch flame contour. The mean value reduces the effect of the occurring cyclic variation and supports the derivation of a more reliable contour as background noise becomes less effective.

Nevertheless, even with the mean value of all recorded images in one cycle, there seems to be no lift-off length between the cap of the unscavenged pre-chamber spark plug and the torch flame, especially for the torch flame 7. With this, the assumption of a predominant flame-based ignition, combustion seems more comprising.

The evaluation of torch flame 7's length shows the interaction with the piston bowl and the in-cylinder flow with an increased reactivity at the tip. The interaction seems similar for both investigated fuels under the reprojection accuracy. The remaining visible torch rays show a predominantly evaluation perpendicular to the flame axis, which ignites the combustion chamber. This seems to be due to the in-cylinder flow and the mounting position.

For the low air–fuel ratio of only two, one image could be captured where a torch flame is visible. This is due to the good ignition and flame propagation conditions in the combustion chamber of the selected experimental point. A higher capture rate seems to be necessary to record the complete development of the torch flame, especially at low air-to-fuel ratios. Both investigated fuels show a similar behavior in the development of the torch flames when comparing intensities and color. This is due to the decreased deviation of both fuel properties, as also stated in [40].

6. Conclusions and Outlook

The paper presents in detail:

- The thermodynamic comparison of the combustion of NG, 5HCH₄ and 10HCH₄ in two test series using an unscavenged pre-chamber spark plug and a conventional spark plug under CoC and air–fuel equivalence ratio variations.
- The optical comparison of the natural chemiluminescence intensity of the combustion of NG, 5HCH₄ and 10HCH₄ using an unscavenged pre-chamber spark plug and a conventional spark plug under a CoC and air–fuel equivalence ratio variation.
- The interpretation of the flame color for NG and 10HCH₄ at two stages of air–fuel equivalence ratio at CoC of 8 °CA aFTDC for both ignition systems.
- A discussion of the visible natural chemiluminescence of the torch flame from images that are post-processed by a virtual reprojection method.

The following conclusions could be derived from the results:

- Hydrogen admixture leads to faster combustion for the unscavenged pre-chamber spark plug compared to pure NG investigations and the tests of the conventional spark plug.
- For a CoC of under 15 °CA aFTDC, the burning duration decreases for both ignition systems and fuels.

- The unscavenged pre-chamber spark plug offers less ignition delay compared to the conventional spark plug. Using the unscavenged pre-chamber spark plugs, the influence of the here-used amount of hydrogen admixture is almost negligible.
- The admixture of hydrogen improves combustion stability. This holds true, especially for the conventional spark plug but has only a minor effect for the unscavenged pre-chamber spark plug.
- The indicated mean efficiency increases with increasing amounts of hydrogen and reaches its maximum for the herein investigated unscavenged pre-chamber spark plug and maximum admixture of hydrogen.
- The apparent heat release rates of both hydrogen admixture levels are of similar quality for each ignition system. In detail, the conventional spark plug shows a slower and less intense heat release compared with the unscavenged pre-chamber spark plug.
- The beneficial effect of the hydrogen admixture becomes especially visible for higher air–fuel equivalence ratios.
- The intensity of the natural chemiluminescence increases mainly in proportion to the air–fuel equivalence ratio and the resulting burn velocity and is at its maximum for low air–fuel equivalence ratios and 10HCH₄ for the tests with the unscavenged pre-chamber spark plug.
- After the thermodynamic end of combustion at MFB95, a remarkable intensity of the natural chemiluminescence remains. The intensity also follows the combustion temperature and can be a hint for thermal excited water.
- The flame coloring at characteristic operation points during combustion (MFB 5, 10, 50, 95) develops proportionally to the intensity trace of the natural chemiluminescence and, thus, also the air–fuel equivalence ratio.
- For lower combustion temperatures at high air–fuel ratios, a higher content of blue is visible in the flame leading to the assumption of a higher emergence of CH* and less overlaid broadband luminosity as well as less C₂* radiation which vanishes for high air–fuel ratios. Further, a slow burn velocity supports the visibility of the CH* emissions.
- High combustion temperatures at low air–fuel ratios result in an intense yellow flame that originates from broadband emissions and those of the C₂* radicals. Due to the low content of the hydrogen admixture at low air–fuel ratios, enough carbon seems available to advance their local formation.
- The end of the combustion shows a more reddish flame concentrated in the center of the combustion chamber, hinting at thermally excited H₂O.

The early stage of combustion using the unscavenged pre-chamber spark plug shows no obvious differences between both fuels concerning the color of the flame and the intensity. Only the influence of the air–fuel equivalence ratio is obvious, resulting in faster combustion with a more yellow flame under fuel-rich conditions.

The correlation of the optical results with the thermodynamic ones shows a reasonable behavior of the combustion. It also proves the feasibility and comparability of the developed alternative fully optically accessible engine and emphasizes the potential of further enhancement to gain more quantitative measurements, e.g., with a similar approach as presented in [23]. Further, the development of a UV-transmission fisheye endoscopic system would support laser-based measurement techniques as well as the observation of the flame's natural OH-chemiluminescence. With such an optic, the testing and development of large-bore engines that can run on pure hydrogen and not only admixtures are possible. It allows the complete decarbonization of combustion engines and thus realizes the usage of a purely sustainable energy supply. Nevertheless, the presented investigations for the admixture of 10%_v to methane shows already several advantages, even for the unscavenged pre-chamber spark plug. With this, a content of 10%_v hydrogen in the natural gas grid seems already feasible from the point of view of stationary energy generation using combined heat and energy plant units, which can be the first step towards sustainable energy generation. Further investigations on the infrastructure of the gas grid are

necessary to avoid risks for other consumers than combustion engines connected to the natural gas grid.

Author Contributions: The optical setup (development and design), as well as the processing and interpretation of the thermodynamic and optical data belonging to S.K. S.E. supported the experiments on the testing rig. The original writing, visualization, writing—review and editing was conducted by S.K. The co-authors M.P., M.J. and G.W. supported the work with internal reviews. All authors have read and agreed to the published version of the manuscript.

Funding: This work has received funding from the German Federal Ministry for Economic Affairs and Energy under funding code 03EIV013B.

Acknowledgments: The authors would like to thank Fabian Liemawan Adji for his support as a student research assistant during the implementation of the pre- and postprocessing algorithms in Matlab.

Conflicts of Interest: The authors declare no conflict of interest.

Nomenclature

aFTDC	After firing top dead center	FTDC	Firing top dead center
aTDC	After top dead center	ICE	Internal combustion engine
bFTDC	Before firing top dead center	IMEP	Indicated mean effective pressure
bTDC	Before top dead center	MFB	Mass fraction burned
CA	Crank angle	NG	Natural gas
CoC	Center of combustion as 50% burnt mass fraction		
CoI	Center of intensities	ROI	Region of interest
COV	Coefficient of variance	SP	Spark plug
DF	Dual fuel	UP-SP	Unscavenged pre-chamber spark plug
EOC	End of combustion	THC	Total hydrocarbon
FOV	Field of view	λ	Air–fuel equivalence ratio
		$\%_V$	Volume percentage

References

- Reitz, R.D.; Ogawa, H.; Payri, R.; Fansler, T.; Kokjohn, S.; Moriyoshi, Y.; Agarwal, A.; Arcoumanis, D.; Assanis, D.; Bae, C.; et al. IJER editorial: The future of the internal combustion engine. *Int. J. Engine Res.* **2020**, *21*, 3–10. [[CrossRef](#)]
- Pöllmann, S.; Härtl, M.; Wachtmeister, G. *Injection Process of the Synthetic Fuel Oxymethylene Ether: Optical Analysis in a Heavy-Duty Engine*; SAE Technical Paper Series; SAE: Warrendale, PA, USA, 2020. [[CrossRef](#)]
- Held, M.; Tönges, Y.; Pélerin, D.; Härtl, M.; Wachtmeister, G.; Burger, J. On the energetic efficiency of producing polyoxymethylene dimethyl ethers from CO₂ using electrical energy. *Energy Environ. Sci.* **2019**, *12*, 1019–1034. [[CrossRef](#)]
- Pélerin, D.; Gaukel, K.; Härtl, M.; Jacob, E.; Wachtmeister, G. Potentials to simplify the engine system using the alternative diesel fuels oxymethylene ether OME1 and OME3–6 on a heavy-duty engine. *Fuel* **2020**, *259*, 116231. [[CrossRef](#)]
- Gelner, A.D.; Höß, R.; Zepf, A.; Härtl, M.; Wachtmeister, G. *Engine Operation Strategies for the Alternative Diesel Fuel Oxymethylene Ether (OME): Evaluation Based on Injection Rate Analyzer and 0D-/1D-Simulation*; SAE Technical Paper Series; SAE: Warrendale, PA, USA, 2021. [[CrossRef](#)]
- Onorati, A.; Payri, R.; Vaglieco, B.; Agarwal, A.; Bae, C.; Bruneaux, G.; Canakci, M.; Gavaises, M.; Günthner, M.; Hasse, C.; et al. The role of hydrogen for future internal combustion engines. *Int. J. Engine Res.* **2022**, *23*, 529–540. [[CrossRef](#)]
- Karmann, S.; Eicheldinger, S.; Prager, M.; Wachtmeister, G. Optical and thermodynamic investigations of a methane and hydrogen blend fueled large bore engine. *Int. J. Engine Res.* **2022**, *23*, 846–864. [[CrossRef](#)]
- Karmann, S.B.; Prager, M.; Wachtmeister, G. Conceptual Investigations on Full Optical Accessibility to Large-Bore Medium-Speed Engines. *SAE Int. J. Engines* **2019**, *12*, 291–308. [[CrossRef](#)]
- Karmann, S.B.; Kunkel, C.; Wachtmeister, G. A New Optical Access for Medium Speed Large Bore Marine Engines under Full-Load Operating Conditions. *SAE Int. J. Engines* **2021**, *14*, 867–883. [[CrossRef](#)]
- Karmann, S.B.; Röhrle, H.; Klier, B.; Prager, M.; Wachtmeister, G. Design of an Endoscopic Fully Optically Accessible High-Speed Large-Bore Engine. *SAE Int. J. Engines* **2022**, *15*, 117193. [[CrossRef](#)]
- Mehra, R.K.; Duan, H.; Juknelevičius, R.; Ma, F.; Li, J. Progress in hydrogen enriched compressed natural gas (HCNG) internal combustion engines—A comprehensive review. *Renew. Sustain. Energy Rev.* **2017**, *80*, 1458–1498. [[CrossRef](#)]
- White, C.; Steeper, R.; Lutz, A. The hydrogen-fueled internal combustion engine: A technical review. *Int. J. Hydrogen Energy* **2006**, *31*, 1292–1305. [[CrossRef](#)]

13. Sahoo, B.; Sahoo, N.; Saha, U. Effect of engine parameters and type of gaseous fuel on the performance of dual-fuel gas diesel engines—A critical review. *Renew. Sustain. Energy Rev.* **2009**, *13*, 1151–1184. [CrossRef]
14. Wahl, J.; Kallo, J. Quantitative valuation of hydrogen blending in European gas grids and its impact on the combustion process of large-bore gas engines. *Int. J. Hydrogen Energy* **2020**, *45*, 32534–32546. [CrossRef]
15. Zhen, X.; Li, X.; Wang, Y.; Liu, D.; Tian, Z. Comparative study on combustion and emission characteristics of methanol/hydrogen, ethanol/hydrogen and methane/hydrogen blends in high compression ratio SI engine. *Fuel* **2020**, *267*, 117193. [CrossRef]
16. Verhelst, S.; Wallner, T. Hydrogen-fueled internal combustion engines. *Prog. Energy Combust. Sci.* **2009**, *35*, 490–527. [CrossRef]
17. Di Sarli, V.; Di Benedetto, A. Laminar burning velocity of hydrogen–methane/air premixed flames. *Int. J. Hydrogen Energy* **2007**, *32*, 637–646. [CrossRef]
18. Stocker, R. Bestimmung Verbrennungsrelevanter Größen in Flammen mit Laseroptischen Verfahren. Ph.D. Thesis, Fakultät für Maschinenwesen, Technische Universität München, München, Germany, 2004.
19. Gaydon, A. *The Spectroscopy of Flames*; Springer: Dordrecht, The Netherlands, 1974. Available online: <https://ebookcentral.proquest.com/lib/kxp/detail.action?docID=6560931> (accessed on 28 December 2022).
20. Oh, S.; Park, Y.; Seon, G.; Hwang, W.; Do, H. Impacts of N₂ and CO₂ diluent gas composition on flame emission spectroscopy for fuel concentration measurements in flames. *Int. J. Heat Mass Transf.* **2020**, *149*, 119174. [CrossRef]
21. Brockhinke, A.; Krüger, J.; Heusing, M.; Letzgus, M. Measurement and simulation of rotationally-resolved chemiluminescence spectra in flames. *Appl. Phys. B Laser Opt.* **2012**, *107*, 539–549. [CrossRef]
22. Karmann, S.; Mühlthaler, M.; Prager, M.; Wachtmeister, G.; Unfug, F. *A Method for Measuring in-Cylinder λ -Distribution in Medium-Speed DF Engines*; Lehrstuhl für Verbrennungskraftmaschinen: Munich, Germany, 2016. Available online: http://www.hercules-2.com/sites/default/files/pub/D2.1_634135_A%20method%20for%20measuring%20in-cylinder%20--distribution%20in%20medium-speed%20DF%20engines.pdf (accessed on 31 January 2017).
23. Sun, Z.; Ma, Z.; Li, X.; Xu, M. Flame Emission Characteristics in a Direct Injection Spark Ignition Optical Engine Using Image Processing Based Diagnostics. In Proceedings of the ASME Internal Combustion Engine Fall Technical Conference—2018: Presented at ASME 2018 Internal Combustion Engine Fall Technical Conference, San Diego, CA, USA, 4–7 November 2018.
24. Warnatz, J.; Maas, U.; Dibble, R.W. *Verbrennung: Physikalisch-Chemische Grundlagen, Modellierung und Simulation, Experimente, Schadstoffentstehung*, 3rd ed.; Springer: Berlin/Heidelberg, Germany, 2001.
25. Catapano, F.; Di Iorio, S.; Sementa, P.; Vaglieco, B.M. Characterization of CH₄ and CH₄/H₂ Mixtures Combustion in a Small Displacement Optical Engine. *SAE Int. J. Fuels Lubr.* **2013**, *6*, 24–33. [CrossRef]
26. García-Armingol, T.; Ballester, J. Flame chemiluminescence in premixed combustion of hydrogen-enriched fuels. *Int. J. Hydrogen Energy* **2014**, *39*, 11299–11307. [CrossRef]
27. Oh, J.; Noh, D.; Ko, C. The effect of hydrogen addition on the flame behavior of a non-premixed oxy-methane jet in a lab-scale furnace. *Energy* **2013**, *62*, 362–369. [CrossRef]
28. Di Iorio, S.; Sementa, P.; Vaglieco, B.M. Experimental investigation on the combustion process in a spark ignition optically accessible engine fueled with methane/hydrogen blends. *Int. J. Hydrogen Energy* **2014**, *39*, 9809–9823. [CrossRef]
29. Di Iorio, S.; Sementa, P.; Vaglieco, B.M. Optical diagnostics for the analysis of hydrogen–methane blend combustion in internal combustion engines. In *Woodhead Publishing Series in Energy, Number 85, Hydrogen Energy Conversion*; Barbir, F., Basile, A., Veziroğlu, T.N., Eds.; Elsevier/WP Woodhead Publishing: Amsterdam, The Netherlands; Boston, MA, USA; Cambridge, UK, 2016; pp. 233–261.
30. Bowditch, F.W. *A New Tool for Combustion Research a Quartz Piston Engine*; SAE Technical Paper; SAE: Warrendale, PA, USA, 1961. [CrossRef]
31. Eicheldinger, S.; Karmann, S.; Prager, M.; Wachtmeister, G. Optical screening investigations of backfire in a large bore medium speed hydrogen engine. *Int. J. Engine Res.* **2021**, *23*, 893–906. [CrossRef]
32. Weber, S.; Stegmann, R.; Prager, M.; Wachtmeister, G. The Effect of Inlet Valve Timing and Engine Speed on Dual Fuel NG-Diesel Combustion in a Large Bore Engine. *SAE Int. J. Engines* **2018**, *11*, 229–246. [CrossRef]
33. Karmann, S.; Eicheldinger, S.; Prager, M.; Jaensch, M.; Wachtmeister, G. Experimental comparison between an optical and an all-metal large bore engine. *Int. J. Engine Res.* **2022**. [CrossRef]
34. Chen, L.; Wei, H.; Zhang, R.; Pan, J.; Zhou, L.; Feng, D. Effects of spark plug type and ignition energy on combustion performance in an optical SI engine fueled with methane. *Appl. Therm. Eng.* **2019**, *148*, 188–195. [CrossRef]
35. Karmann, S.B.; Weber, S.; Stürzl, W.; Prager, M.; Jaensch, M.; Wachtmeister, G. Development of an Optical Investigation Method for Diesel and Oxymethylene Ether Spray in a Large-Bore Dual-Fuel Engine Using a Fisheye Optical System. *SAE Int. J. Engines* **2023**, *16*. [CrossRef]
36. Dong, C.; Zhou, Q.; Zhang, X.; Zhao, Q.; Xu, T.; Hui, S. Experimental study on the laminar flame speed of hydrogen/natural gas/air mixtures. *Front. Chem. Eng. China* **2010**, *4*, 417–422. [CrossRef]
37. Röthlisberger, R. An Experimental Investigation of a Lean Burn Natural Gas Prechamber Spark Ignition Engine for Cogeneration. 2005. Available online: https://infoscience.epfl.ch/record/32822/files/EPFL_TH2346.pdf (accessed on 27 December 2022).
38. Park, C.; Kim, C.; Choi, Y.; Won, S.; Moriyoshi, Y. The influences of hydrogen on the performance and emission characteristics of a heavy duty natural gas engine. *Int. J. Hydrogen Energy* **2011**, *36*, 3739–3745. [CrossRef]
39. Kannala, J.; Heikkilä, J.; Brandt, S.S. Geometric Camera Calibration. *Wiley Encycl. Comput. Sci. Eng.* **2008**, *13*, 1–12.

40. Strobl, K.H.; Sepp, W.; Fuchs, S.; Paredes, C.; Smisek, M.; Arbter, K. DLR CalDe and DLR CalLab. Oberpfaffenhofen, Germany. Available online: <http://www.robotic.dlr.de/callab/> (accessed on 27 December 2022).
41. Greis, E.A. Laseroptische Untersuchungen des Verbrennungsprozesses in Einem PKW-Dieselmotor. Ph.D. Thesis, Fakultät für Maschinenwesen, Rheinisch-Westfälische Technische Hochschule, Aachen, Germany, 2007.
42. Geßenhardt, C. Endoskopische Bestimmung des Temperaturfeldes im Brennraum von Ottomotoren mittels laserinduzierter Fluoreszenz. Ph.D. Dissertation, Universität Duisburg-Essen, Fakultät für Ingenieurwissenschaften, Abteilung Maschinenbau, Duisburg, Germany, 2013.
43. Nilsson, E.J.; van Sprang, A.; Larfeldt, J.; Konnov, A.A. The comparative and combined effects of hydrogen addition on the laminar burning velocities of methane and its blends with ethane and propane. *Fuel* **2017**, *189*, 369–376. [[CrossRef](#)]
44. García-Armingol, T.; Ballester, J. Influence of fuel composition on chemiluminescence emission in premixed flames of CH₄/CO₂/H₂/CO blends. *Int. J. Hydrogen Energy* **2014**, *39*, 20255–20265. [[CrossRef](#)]
45. Ballester, J.; Hernández, R.; Sanz, A.; Smolarz, A.; Barroso, J.; Pina, A. Chemiluminescence monitoring in premixed flames of natural gas and its blends with hydrogen. *Proc. Combust. Inst.* **2009**, *32*, 2983–2991. [[CrossRef](#)]
46. Korb, B. Beitrag zur Charakterisierung des Homogenen Magerbrennverfahrens bei Großgasmotoren mittels Experimenteller Methoden im Hinblick auf Verbrennung, Wirkungsgrad und Emissionen. Ph.D. Thesis, TUM School of Engineering and Design, Technische Universität München, München, Germany, 2021.
47. Xu, G.; Kotzagianni, M.; Kyrtatos, P.; Wright, Y.M.; Boulouchos, K. Experimental and numerical investigations of the unscavenged prechamber combustion in a rapid compression and expansion machine under engine-like conditions. *Combust. Flame* **2019**, *204*, 68–84. [[CrossRef](#)]

Disclaimer/Publisher’s Note: The statements, opinions and data contained in all publications are solely those of the individual author(s) and contributor(s) and not of MDPI and/or the editor(s). MDPI and/or the editor(s) disclaim responsibility for any injury to people or property resulting from any ideas, methods, instructions or products referred to in the content.